

Reversing a model of Parkinson's disease with in situ converted nigral neurons

<https://doi.org/10.1038/s41586-020-2388-4>

Received: 12 November 2018

Accepted: 13 May 2020

Published online: 24 June 2020

 Check for updates

Hao Qian¹, Xinjiang Kang^{2,3}, Jing Hu^{1,8}, Dongyang Zhang⁴, Zhengyu Liang¹, Fan Meng¹, Xuan Zhang¹, Yuanchao Xue^{1,9}, Roy Maimon^{1,5}, Steven F. Dowdy¹, Neal K. Devaraj⁴, Zhuan Zhou², William C. Mobley⁶, Don W. Cleveland^{1,5} & Xiang-Dong Fu^{1,7}✉

Parkinson's disease is characterized by loss of dopamine neurons in the substantia nigra¹. Similar to other major neurodegenerative disorders, there are no disease-modifying treatments for Parkinson's disease. While most treatment strategies aim to prevent neuronal loss or protect vulnerable neuronal circuits, a potential alternative is to replace lost neurons to reconstruct disrupted circuits². Here we report an efficient one-step conversion of isolated mouse and human astrocytes to functional neurons by depleting the RNA-binding protein PTB (also known as PTBP1). Applying this approach to the mouse brain, we demonstrate progressive conversion of astrocytes to new neurons that innervate into and repopulate endogenous neural circuits. Astrocytes from different brain regions are converted to different neuronal subtypes. Using a chemically induced model of Parkinson's disease in mouse, we show conversion of midbrain astrocytes to dopaminergic neurons, which provide axons to reconstruct the nigrostriatal circuit. Notably, re-innervation of striatum is accompanied by restoration of dopamine levels and rescue of motor deficits. A similar reversal of disease phenotype is also accomplished by converting astrocytes to neurons using antisense oligonucleotides to transiently suppress PTB. These findings identify a potentially powerful and clinically feasible approach to treating neurodegeneration by replacing lost neurons.

Regenerative medicine holds great promise for treatment of disorders that feature loss of cells³. Given the plasticity of certain somatic cells⁴, transdifferentiation approaches for switching cell fate in situ—thereby avoiding immune recognition—have gained momentum². In the mouse brain, glial cell plasticity⁵ has been leveraged to generate new neurons that lead to behavioural benefits in disease models^{6,7}. However, there is limited evidence for transdifferentiated cells replacing lost neurons to reconstitute an endogenous neuronal circuit⁸.

Most in vivo reprogramming relies on using lineage-specific transcription factors. We recently identified roles for the RNA-binding protein PTB and its neuronal analogue nPTB in controlling neuronal induction and maturation and demonstrated efficient conversion of mouse and human fibroblasts to functional neurons by sequential depletion of these RNA-binding proteins^{9,10}. Notably, sequential downregulation of PTB and nPTB occurs naturally during neurogenesis¹¹, and once triggered, both PTB- and nPTB-regulated gene expression loops become self-reinforcing^{9,10}.

In this study, we investigate this strategy to directly convert astrocytes to dopaminergic (DA) neurons in the substantia nigra. Using a chemically induced model of Parkinson's disease in mouse, we show that dopamine neurons induced by PTB depletion potently restore

striatal dopamine, reconstitute the nigrostriatal circuit, and reverse Parkinson's disease-like motor phenotypes. Given the emerging power of antisense oligonucleotides (ASOs) in modulating brain disorders¹², we also provide evidence for the use of ASOs directed against *PTBP1* (the gene that encodes PTB) as a feasible, single-step strategy for treating Parkinson's disease and perhaps other neurodegenerative diseases.

PTB- and nPTB-regulated loops in astrocytes

Astrocytes offer several advantages for in vivo reprogramming in the brain. These non-neuronal cells are abundant, proliferate upon injury, and are highly plastic with regards to cell fate⁵. As previously established in fibroblasts^{9,10}, PTB suppresses a neuronal induction loop in which the microRNA miR-124 inhibits the transcriptional repressor REST that suppresses many neuronal genes, including miR-124 (Fig. 1a, loop 1). Downregulation of PTB induces expression of nPTB, which suppresses the transcription activator BRN2 and the microRNA miR-9, both of which are required for neuronal maturation (Fig. 1a, loop 2). By modulating both loops, sequential downregulation of PTB and nPTB generates functional neurons from human fibroblasts¹⁰.

¹Department of Cellular and Molecular Medicine, University of California, San Diego, La Jolla, CA, USA. ²State Key Laboratory of Membrane Biology and Institute of Molecular Medicine, Peking University, Beijing, China. ³MOE Key Lab of Medical Electrophysiology, ICR, Southwest Medical University, Luzhou, China. ⁴Department of Chemistry and Biochemistry, University of California, San Diego, La Jolla, CA, USA. ⁵Ludwig Institute for Cancer Research, University of California, San Diego, La Jolla, CA, USA. ⁶Department of Neurosciences and Center for Neural Circuits and Behavior, University of California, San Diego, La Jolla, CA, USA. ⁷Institute of Genomic Medicine, University of California, San Diego, La Jolla, CA, USA. ⁸Present address: Sichuan Provincial Key Laboratory for Human Disease Gene Study, Sichuan Provincial People's Hospital, University of Electronic Science and Technology of China, Chengdu, China. ⁹Present address: Key Laboratory of RNA Biology, Institute of Biophysics, Chinese Academy of Sciences, Beijing, China. ✉e-mail: xdfu@ucsd.edu

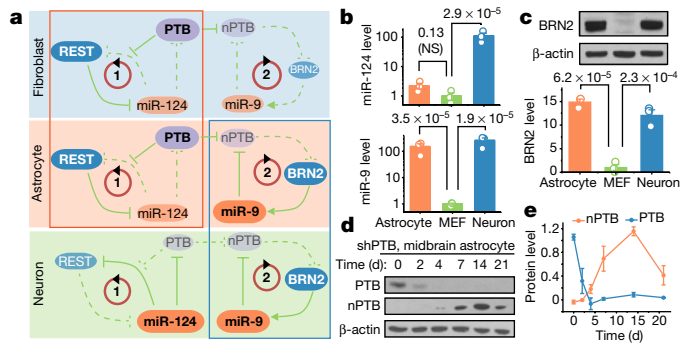


Fig. 1 | PTB knockdown induces neurogenesis in mouse and human astrocytes. **a**, PTB and nPTB-regulated loops critical for neuronal induction and maturation in fibroblasts, astrocytes and neurons. Bold text indicates increased expression level. The red box highlights similarity between fibroblasts and astrocytes in the PTB-regulated loop; the blue box highlights similarity between astrocytes and neurons in the nPTB-regulated loop. **b**, RT-qPCR of miR-124 and miR-9, normalized against U6 snRNA in mouse astrocytes, mouse embryonic fibroblasts (MEFs) and mouse neurons. **c**, Western blot and quantification of BRN2, normalized against β -actin in mouse astrocytes, MEFs and mouse neurons. In **b**, **c**, data are mean \pm s.e.m. ($n = 3$ biological repeats); P -values by ANOVA with post hoc Tukey test. NS, not significant. **d**, **e**, Western blot (**d**) and quantification (**e**) of nPTB levels following PTB knockdown in mouse midbrain astrocytes. $n = 3$ biological repeats. Data are mean \pm s.e.m.

To investigate this cascade in the conversion of astrocytes to neurons, we used mouse astrocytes from the cerebral cortex and midbrain of postnatal day (P)4 to P5 pups¹³ and human fetal cortical astrocytes from gestational week 19. These cells express the astrocyte markers GFAP and ALDH1L1, but not markers for neurons and other common non-neuronal cell types in the brain (Extended Data Fig. 1a). Similar to fibroblasts, analysis by quantitative PCR with reverse transcription (RT-qPCR) showed low levels of miR-124 in the mouse and human astrocytes (Fig. 1b, Extended Data Fig. 1b). Unexpectedly, both miR-9 and BRN2 were highly expressed in astrocytes (Fig. 1b, c, Extended Data Fig. 1c). We further confirmed these expression patterns in endogenous astrocytes and neurons (Extended Data Fig. 1d). Note that expression of REST is decreased, but not eliminated, in DA neurons marked by tyrosine hydroxylase (TH), consistent with its requirement for sustaining the viability of mature neurons in the brain¹⁴. Thus, the PTB-regulated loop in astrocytes resembles the one in fibroblasts (Fig. 1a, red box), and the nPTB-regulated loop in astrocytes resembles the one in neurons (Fig. 1a, blue box). We therefore proposed that nPTB induced by PTB knockdown would be immediately counteracted by miR-9 in astrocytes, as seen during neurogenesis from neural stem cells¹⁵. Indeed, unlike human dermal fibroblasts, PTB-deficient astrocytes showed transient nPTB induction (Fig. 1d, e, Extended Data Fig. 1e, f). These results suggest that astrocytes can be converted to neurons by PTB knockdown alone in both mice and humans.

Efficient astrocyte conversion in vitro

To demonstrate the functionality of converted neurons, we transduced mouse cortical astrocytes with a lentivirus expressing a small hairpin RNA (shRNA) against *Ptbp1* (shPTB). After four weeks, 50 to 80% of shPTB-transduced cells showed neuronal morphology and stained positive for the pan-neuronal markers TUJ1 and MAP2, whereas transduction with control virus did not cause expression of these markers (Fig. 2a). RNA-sequencing (RNA-seq) analysis was performed before and after conversion (Supplementary Table 1) and compared to public gene expression profiles of astrocytes and neurons (Extended Data Fig. 2a). This showed a degree of heterogeneity between independent

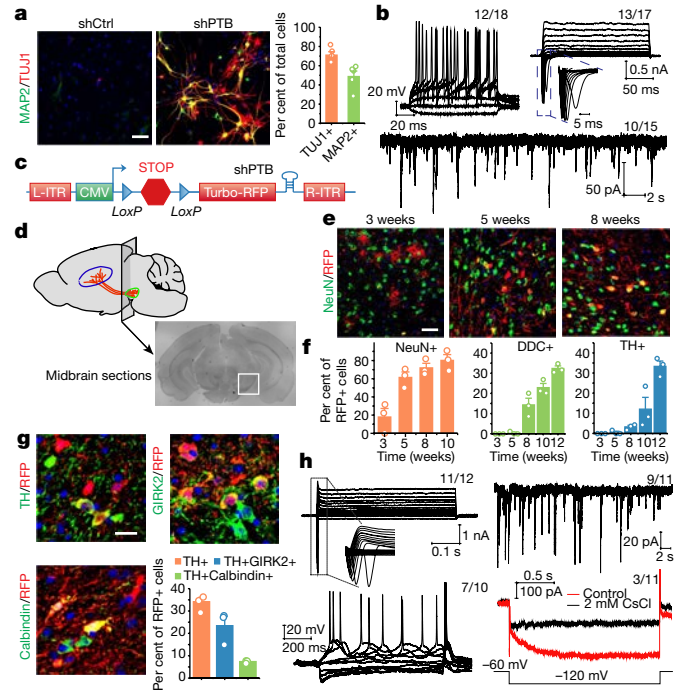


Fig. 2 | Conversion of astrocytes to functional neurons in vitro and in mouse brain. **a**, Left, cortical astrocytes, treated with shCtrl or shPTB lentivirus, were stained for TUJ1 (red) and MAP2 (green). Scale bar, 80 μ m. Right, quantification of the numbers of cells stained with each marker ($n = 5$ biological repeats). Data are mean \pm s.e.m. **b**, Electrophysiological recordings, showing repetitive action potentials (top left), large currents of voltage-dependent sodium and potassium channels (top right), and spontaneous postsynaptic currents after co-culture with rat astrocytes (bottom). Indicated in each panel is the number of cells that showed the recorded activity versus the total number of cells examined. **c**, Design of the AAV-shPTB vector. AAV-empty is the same but without shPTB. **d**, Schematic of the midbrain section used for immunohistochemical analysis in **e**–**h**. **e**, Gradual conversion of midbrain astrocytes to NeuN+ neurons. Representative images at three time points. Scale bar, 35 μ m. **f**, Number of RFP+ cells from **e** that show positive staining for NeuN (left), DDC (middle) and TH (right). $n = 3$ biological repeats. Data are mean \pm s.e.m. **g**, Converted TH+ DA neurons marked by GIRK2 or calbindin. Scale bar, 20 μ m. Bottom right, results from three mice were quantified. Data are mean \pm s.e.m. **h**, Electrophysiological recordings on brain slices, showing large currents from voltage-dependent sodium and potassium channels (top left), spontaneous postsynaptic currents (top right), repetitive action potentials (bottom left) and mature DA neuron-associated HCN channel activities, which are specifically blocked with 2 mM CsCl (bottom right). Indicated in each panel is the number of cells that showed the recorded activity versus the total number of cells examined.

isolates of cortical or midbrain astrocytes, but both isolates produced more homogeneous transcriptomes following conversion to neurons (Extended Data Fig. 2b, c). During conversion, typical astrocyte genes were suppressed, whereas neuronal genes were induced (Extended Data Fig. 2b, c). Notably, midbrain astrocytes gave rise to neurons expressing many DA neuron-specific genes (Extended Data Fig. 2d).

Mouse and human astrocyte-derived neurons were positive for NeuN and NSE, and most expressed markers of glutamatergic (VGLut1) or GABA (γ -aminobutyric acid)-containing (GABAergic) neurons (GAD67) (Extended Data Fig. 3a, b). Patch clamp recording six to eight weeks after conversion showed currents of voltage-gated sodium and potassium channels and repetitive action potential firing in neurons derived from both mouse and human astrocytes, and—by co-culturing the converted neurons with freshly isolated rat astrocytes—spontaneous postsynaptic events of varying frequencies were also recorded (Fig. 2b, Extended Data Fig. 3c, d). Sequential addition of antagonists of

ionotropic glutamatergic receptors (NBQX and APV) and an antagonist of GABA_A receptors (picrotoxin (PiTX)) blocked the signals, indicating that the converted neurons respond to synaptic inputs from both glutamatergic and GABAergic neurons. No neuronal electrophysiological properties were detectable in astrocytes transduced with control virus (Extended Data Fig. 3e–h). These results demonstrate a one-step conversion to functional neurons by depletion of PTB.

Generating new neurons in mouse brain

We next attempted to directly reprogram astrocytes into neurons in the mouse brain. We designed an adeno-associated virus (AAV; serotype 2) vector to express shPTB (AAV-shPTB) (Fig. 2c) and a corresponding empty vector lacking shPTB (AAV-empty) as control. To enable lineage tracing, 5' to the shPTB hairpin, we placed a red fluorescent protein (RFP)-coding sequence that was initially silenced (by a *loxP*-Stop-*loxP* cassette) but activated in cells expressing Cre recombinase. Focusing on the substantia nigra of the midbrain where DA neurons reside (Fig. 2d), we found that RFP+ cells were almost completely absent 10 weeks after injecting either AAV-empty or AAV-shPTB in wild-type mice at 1 to 2 months of age, a developmental stage when astrocytes have already lost their neurosphere-generating potential in the midbrain¹⁶. By contrast, RFP was expressed in response to both AAVs in *Gfap-cre* transgenic mice expressing Cre recombinase from the astrocyte-specific *Gfap* promoter¹⁷ (Extended Data Fig. 4a, b).

Ten weeks after injection of AAV-empty into substantia nigra, most RFP+ cells were astrocytes, as indicated by typical astrocytic morphology and expression of the astrocyte markers S100b and ALDH1L1 (Extended Data Fig. 4c), with no evidence for viral transduction in NG2 cells (Extended Data Fig. 4d). We detected RFP in about 1% of NeuN+ neurons (Extended Data Fig. 4e), demonstrating minimal Cre expression in endogenous neurons in young adult mice. By contrast, 3 weeks after AAV-shPTB injection, around 20% of RFP+ cells expressed NeuN; the percentage of RFP+NeuN+ cells more than tripled by 5 weeks; and by 10 weeks around 80% of RFP+ cells were NeuN+GFAP- (Fig. 2e, f, Extended Data Fig. 4e). At this time point, most converted neurons also expressed multiple mature neuron markers (for example, MAP2, NSE and PSD95) (Extended Data Fig. 4f) and markers for glutamatergic (VGLut2) or GABAergic (GAD65) neurons (Extended Data Fig. 4g). These results demonstrate shPTB-mediated, time-dependent astrocyte-to-neuron conversion in the mouse midbrain.

Progressive maturation of new DA neurons

We next monitored the gradual appearance of DA neurons among RFP-labelled cells from 3 to 12 weeks after AAV-shPTB injection in the midbrain (Fig. 2e, f). On the basis of staining with the DA neuron markers DOPA decarboxylase (DDC) and TH, we detected a progressive increase in the number of converted DA neurons, which reached 30–35% of RFP+ cells 12 weeks after injection (Fig. 2f, Extended Data Fig. 5a, b). All RFP+TH+ DA neurons were detected proximal to, but not distal from, the site of injection where endogenous TH+RFP- DA neurons reside (Extended Data Fig. 5c–e), indicating restricted astrocyte-to-DA neuron conversion within the dopamine domain. Converted neurons also expressed multiple DA neuron markers, such as DAT, VMAT2, EN1, LMX1A and PITX3 (Extended Data Fig. 5f), with morphology similar to that of endogenous DA neurons (Extended Data Fig. 5g). A substantial population of RFP+ cells (about 22% of RFP+ cells) expressed TH and GIRK2 (a marker of A9 DA neurons and a subpopulation of A10 neurons), whereas a minor population (about 7% of RFP+ cells) expressed TH and calbindin-D28k (a marker of A10 DA neurons) (Fig. 2g), indicating that different subtypes of DA neurons were generated. Furthermore, SOX6-marked RFP+ DA neurons were confined to the substantia nigra and OTX2-marked RFP+ DA neurons were confined to the ventral tegmental area (VTA); both types expressed a common DA neuron marker,

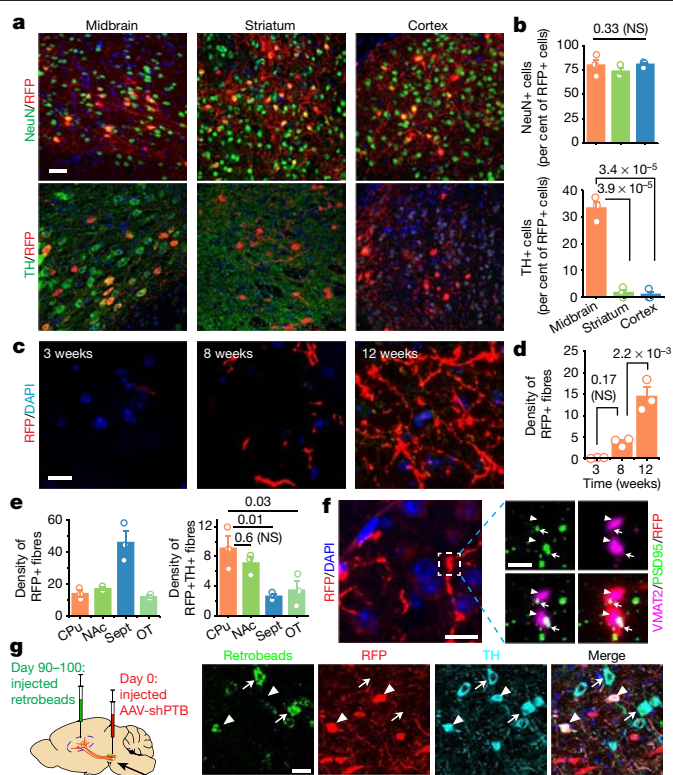


Fig. 3 | Regional specificity in astrocyte-to-neuron conversion and axonal targeting. **a, b**, Induction of NeuN+ neurons in three brain regions, showing that TH+ neurons were detected only in the midbrain. Scale bar, 40 μ m. $n = 3$ mice. **c, d**, Progressive targeting of RFP+ fibres to striatum over the course of 12 weeks. Scale bar, 10 μ m. RFP+ fibre density was determined by the sphere method and quantified (**d**) from images (**c**) at each time point. $n = 3$ biological repeats. **e**, Targeting of RFP+ fibres to multiple subregions around the striatum, particularly septal nuclei (sept) (left), but RFP+TH+ fibres are targeted mainly to CPu and NAC (right). Quantification was performed on images collected at week 12. $n = 3$ mice. **f**, Evidence for synaptic connection in CPu, as indicated in the magnified inset by colocalization of the presynaptic marker VMAT2 (arrowheads) and the postsynaptic marker PSD95 (arrows) on RFP+ fibres. Scale bar, 10 μ m; magnified inset, 2 μ m. **g**, Labelling of RFP+TH+ cells in substantia nigra with retrograde beads injected into striatum 90–100 days after reprogramming (left). Arrowheads indicate converted cells, one of which was labelled by the beads; arrows show endogenous (TH+RFP-) DA neurons labelled by the beads. Scale bar, 20 μ m. In **b, d, e**, ANOVA with post hoc Tukey test; data are mean \pm s.e.m. NS, not significant. P -values are indicated. In **f, g**, three independently repeated experiments with similar results.

ALDH1A1 (Extended Data Fig. 5h–j). No RFP+TH+ cells were detected following injection with AAV-empty (Extended Data Fig. 5k).

Patch clamp recordings of these converted neurons (illustrated in Extended Data Fig. 6a, b) showed typical voltage-dependent currents of sodium and potassium channels, repetitive action potential firing and spontaneous postsynaptic currents. We also recorded the activity of hyperpolarization-active and cyclic nucleotide-gated (HCN) channels that could be specifically blocked with CsCl (Fig. 2h) and relatively wider action potentials compared to those of GABAergic neurons (Extended Data Fig. 6c, d)—both characteristics of mature DA neurons^{18,19}. We recorded no HCN channel activities and rather infrequent firing of spontaneous action potentials at 6 weeks, and found HCN activities and increased firing of spontaneous action potentials in a fraction of RFP+TH+ DA neurons 12 weeks after injection (Extended Data Fig. 6e–g). These results demonstrate progressive functional maturation of new DA neurons within the dopaminergic neuron-containing domain of the midbrain.

Regional specificity in neuronal conversion

As controls for neuronal conversion in midbrain, we additionally injected AAV-shPTB into the cortex and striatum. While the overall conversion efficiency—based on RFP+NeuN+ cells—was similar in these three brain regions, RFP+TH+ DA neurons were detected mainly in the midbrain (Fig. 3a, b) and RFP+CTIP2+ or RFP+CUX1+ neurons were detected mostly in the cortex (Extended Data Fig. 6h). This apparent regional specificity agrees with the RNA-seq data showing that astrocytes from different brain regions exhibited different gene expression programs²⁰. In our culture models, we treated cortical astrocytes with lentiviral shPTB, resulting in around 2% of cells becoming TH+ neurons, as additionally characterized by induction of the DA neuron-specific genes *Slc6a3* and *Foxa2* and positive staining for DAT, VMAT2, TH, LMX1A, PITX3 and DDC (Extended Data Fig. 7a–d). By contrast, cultured midbrain-derived astrocytes produced a fivefold higher proportion (around 10%) of TH+ neurons (Extended Data Fig. 7e–g).

We found no evidence that conditioned medium from cultured midbrain astrocytes enhanced the conversion of cortical astrocytes to TH+ neurons (Extended Data Fig. 8a, b), which prompted us to investigate other potential cell-autonomous contributions to the regional specificity by performing RT-qPCR analysis on isolated cortical and midbrain astrocytes. Relative to cortical astrocytes, midbrain astrocytes expressed higher basal levels of transcription factors enriched in DA neurons (Extended Data Fig. 8c, d) and, in response to PTB depletion, these transcription factors were more robustly induced in midbrain astrocytes relative to cortical astrocytes (Extended Data Fig. 8e, f). These findings suggest that distinct promoter–enhancer networks may underlie the regional specificity for astrocytes from different brain regions, as recently observed in microglia²¹. The higher DA neuron conversion rate also enabled us to record dopamine release from midbrain astrocyte-derived neurons (Extended Data Fig. 8g–i). These *in vitro* studies strongly suggest that higher basal levels and more robust induction of lineage-specific transcription factors may contribute to the higher propensity of midbrain astrocytes to generate DA neurons. The much higher conversion efficiency in the mouse midbrain (about 35%) compared with isolated midbrain astrocytes (about 10%) also points to the contribution of the local microenvironment to DA neuron conversion from midbrain astrocytes.

Innervation in the nigrostriatal pathway

We next investigated the dynamics of fibre outgrowth from newly converted neurons in the brain. We initially monitored the outgrowth of RFP+ fibres along the nigrostriatal bundle (Extended Data Fig. 9a, b). Using the sphere method²², we quantified the fibre density, revealing a time-dependent appearance of RFP+ fibres in the nigrostriatal bundle, reaching 29.6 ± 5.4 fibres by 12 weeks, with 5.75 ± 0.5 fibres being RFP+TH+ (Extended Data Fig. 9c, d) (mean \pm s.e.m.). As DA neurons usually target striatum, we also detected progressively increasing numbers of RFP+ fibres in this distal region, reaching 14.5 ± 3.6 fibres per area by 12 weeks (Fig. 3c, d). Examining brain regions more broadly, we found that RFP+ fibres targeted caudate putamen (CPU) as well as nucleus accumbens (NAc), septal nuclei and olfactory tubercle (Extended Data Fig. 9e), as previously observed with grafted neuronal stem cells²². A fraction of these RFP+ fibres were also TH+ (Extended Data Fig. 9f). Of note, despite around threefold more RFP+ fibres in septal nuclei, RFP+TH+ processes were about fourfold more abundant in both CPU and NAc regions (Fig. 3e). Focusing on the CPU, we detected colocalization of the presynaptic marker VMAT2 and the postsynaptic marker PSD95 on RFP+ fibres, suggesting the presence of synaptic connections (Fig. 3f).

To further substantiate functional targeting to striatum, we injected green fluorescent retrobeads into the CPU region of mice 1 month or 3 months after AAV-shPTB delivery to enable axonal uptake and retrograde labelling of the corresponding cell bodies (Fig. 3g, left). One day

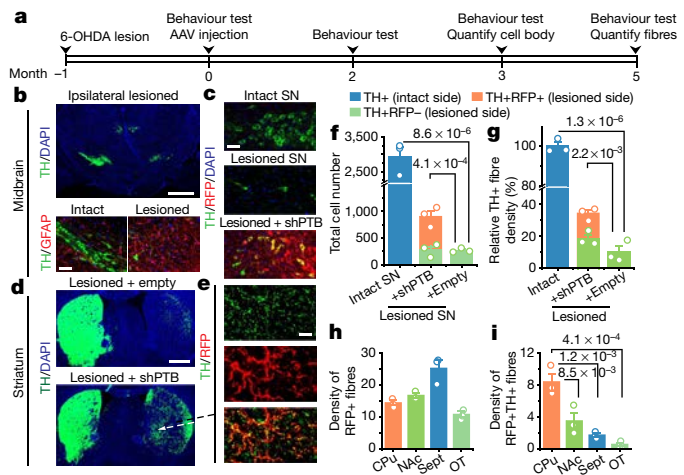


Fig. 4 | Replenishing lost DA neurons to reverse parkinsonian phenotype.

a, Schematic of the experimental schedule for 6-OHDA-induced lesion in substantia nigra (SN) followed by AAV-shPTB treatment and behavioural tests. **b**, Unilateral loss of TH+ cells in midbrain induced by 6-OHDA (top; scale bar, 500 μ m) with increased numbers of GFAP+ astrocytes (bottom; scale bar, 50 μ m). **c**, Comparison between unlesioned (top) and 6-OHDA-lesioned after AAV-shPTB treatment (middle), showing converted DA neurons (yellow) after AAV-shPTB treatment (bottom). Scale bar, 50 μ m. **d, e**, TH+ fibres in striatum treated with AAV-empty (top) or AAV-shPTB (bottom). Scale bar, 500 μ m. **e**, Magnified views from **d**, showing extensive RFP+TH+ fibres. Scale bar, 10 μ m. **b–e**, three independently repeated experiments with similar results. **f, g**, Quantification of cell bodies (**f**) and fibres (**g**) in DA neurons in the unlesioned side (blue), remaining endogenous RFP–TH+ DA neurons in the lesioned side (green), and converted RFP+TH+ DA neurons in the lesioned side (orange). Data were from two sets of mice ($n = 3$ in each set) transduced with AAV-shPTB or AAV-empty. **h, i**, Quantification of RFP+ (**h**) or RFP+TH+ (**i**) fibre density in the indicated subregions of the brain ($n = 3$ mice in each group). OT, olfactory tubercle. In **f, g, i**, ANOVA with post hoc Tukey test; data are mean \pm s.e.m. P -values are indicated.

after injection, we saw green retrobeads in both endogenous TH+RFP– cells and converted TH+RFP+ cells in the substantia nigra. We could detect labelling of only endogenous DA neurons after 1 month following AAV-shPTB transduction (Extended Data Fig. 9g, h), and after 3 months, we detected retrobeads in both endogenous (RFP–) and newly converted (RFP+TH+) neurons (Fig. 3g). These results demonstrate time-dependent incorporation of new DA neurons into the nigrostriatal pathway.

Replenishing lost DA neurons in a disease model

Following the successful generation of DA neurons, we investigated their potential to reconstitute an injured nigrostriatal pathway. We selected a widely used model of Parkinson’s disease in mouse, in which DA neurons are efficiently ablated by 6-hydroxydopamine (6-OHDA), a dopamine analogue that is toxic to DA neurons²³. Although this model does not recapitulate all essential features of Parkinson’s disease pathogenesis²⁴, it does result in a critical endpoint—the loss of neurons in the substantia nigra and depletion of striatal dopamine. One month after 6-OHDA injection into one side of the medial forebrain bundle (Fig. 4a), we observed unilateral loss of TH+ cell bodies in the midbrain (Fig. 4b, top), accompanied by a marked increase in GFAP+ astrocytes (Fig. 4b, bottom), indicative of the expected astrocytic response²⁵. One month after the lesion, we injected AAV-empty or AAV-shPTB in the lesioned side and observed increased RFP+TH+ cell bodies around 10–12 weeks later with AAV-shPTB, but not with AAV-empty (Fig. 4c, Extended Data Fig. 10). We also detected a marked increase in RFP+TH+ fibres in striatum of mice treated with AAV-shPTB, but not in those treated with AAV-empty (Fig. 4d, e, Extended Data Fig. 11a, b).

Quantitative analysis revealed that the initial $2,926 \pm 273$ TH+ neuronal cell bodies in substantia nigra were reduced by around 90% (to 266 ± 22) following the lesion and AAV-shPTB induced 634 ± 38 new RFP+TH+ neurons (Fig. 4f), thereby restoring TH+ neurons to approximately one third (904 ± 108) of the initial number. Similarly, 6-OHDA lesioning reduced the number of TH+ fibres by around 90% and AAV-shPTB restored total TH+ fibre density to about 30% of the density in the uninjured brain (Fig. 4g). We detected a slight increase in TH+RFP- fibre density following treatment with AAV-shPTB compared with AAV-empty (Extended Data Fig. 11c, d), suggesting that AAV-shPTB treatment might aid recovery of some remaining damaged endogenous DA neurons. Quantification of total RFP+ fibres versus RFP+TH+ fibres in different striatal regions and surrounding areas revealed that while the septal nuclei was enriched with RFP+ fibres (Fig. 4h), the CPu contained the highest proportion of RFP+TH+ fibres (Fig. 4i, Extended Data Fig. 12). Thus, without additional treatment to specify neuronal subtypes, AAV-shPTB is sufficient to induce new DA neurons from endogenous midbrain astrocytes that partially restore lost DA neurons and their axons within the nigrostriatal dopamine pathway.

Restoration of striatal dopamine

We next investigated whether AAV-shPTB-induced neurons would restore dopamine levels in the striatum by preparing extracts and quantifying dopamine levels using high-performance liquid chromatography (HPLC) (Fig. 5a). Samples were spiked with known quantities of dopamine to define the elution position and to establish the relationship between signal intensities and the amount of dopamine (Extended Data Fig. 13a, b). We detected similar amounts of dopamine in both sides of uninjured mice (Fig. 5b) and found that 6-OHDA lesion reduced dopamine to about 25% of the normal level (Fig. 5c). Treatment with AAV-shPTB, but not with AAV-empty, markedly increased the dopamine level compared with lesioned striatum (Fig. 5d), reaching approximately 65% of the uninjured level (Fig. 5e).

To test whether DA neuron function was restored, we directly measured activity-induced dopamine release to demonstrate restored DA neuron functions by inserting a stimulating electrode in the medial forebrain bundle and a carbon fibre electrode in striatum of live mice (Fig. 5f). In lesioned mice treated with AAV-empty, we recorded stimulation-dependent dopamine release in the uninjured side but a greatly diminished signal in the lesioned side (Fig. 5g, left). In lesioned mice treated with AAV-shPTB, activity-induced dopamine release was detected in both the uninjured and lesioned sides (Fig. 5g, right). Three out of four mice showed significant restoration of dopamine release (Fig. 5h). Placing a stimulating electrode and carbon fibre electrode on striatal slices from the same group of mice (Fig. 5i), we recorded activity-induced dopamine release (Fig. 5j), with the same mouse showing reduced release as in live recording (Fig. 5k), ruling out a misplaced electrode as a cause of reduced release in vivo. These data demonstrate robust restoration of striatal dopamine and activity-induced dopamine release in AAV-shPTB-reprogrammed mice.

Reversing disease-relevant motor phenotypes

Next, we tested the ability of AAV-shPTB to restore motor function to mice with 6-OHDA lesions. We performed three common behavioural tests, two based on drug-induced rotation and one based on spontaneous motor activities²⁶. Contralateral rotation induced by apomorphine and ipsilateral rotation triggered by amphetamine were markedly increased following lesion with 6-OHDA; both phenotypes were progressively restored to nearly wild-type levels within three months after AAV-shPTB treatment (Fig. 6a, b). No correction was recorded in mice treated with AAV-empty (Fig. 6a) or with non-specific AAV-shGFP (Extended Data Fig. 13c).

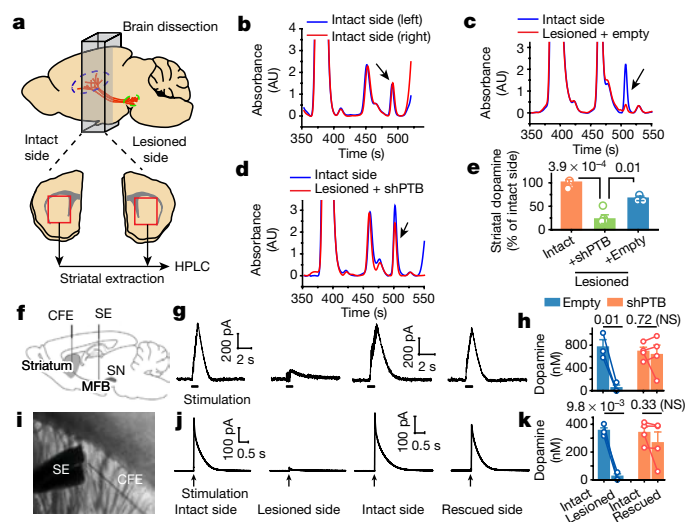


Fig. 5 | Restoration of dopamine biogenesis and activity-induced dopamine release. **a**, Schematic depiction of the measurement of striatal dopamine levels by HPLC. **b–d**, Striatal dopamine levels in two sides of uninjured mouse brain (**b**), comparison between uninjured and 6-OHDA-lesioned sides (**c**) and restoration in the lesioned side after reprogramming in ipsilateral nigra (**d**). Arrows in each panel indicate the position of dopamine in the HPLC profile. AU, absorbance units. **e**, Striatal dopamine restoration after reprogramming with AAV-shPTB in ipsilateral substantia nigra ($n = 3$ uninjured mice or lesioned mice treated with AAV-shPTB; $n = 4$ lesioned mice treated with AAV-empty). **f–h**, Activity-induced dopamine release in striatum. **f**, Schematic of striatal dopamine recording with insertion of a carbon fibre electrode (CFE) in striatum and stimulation electrode (SE) in the medial forebrain bundle (MFB) next to the substantia nigra in live mice. **g**, Representative traces of activity-induced dopamine release recorded on the uninjured and 6-OHDA-lesioned striatum before and after neuronal conversion. **h**, Overall recorded results ($n = 3$ for AAV-empty; $n = 4$ for AAV-shPTB). Circles represent individual mice; lines connect recordings from the same mice before and after reprogramming. **i–k**, Dopamine release in striatal slices from the same set of mice analysed in **g**, as shown in **i**. Representative traces (**j**) and overall results (**k**). In **e**, ANOVA with post hoc Tukey test; in **h, k**, Student's *t*-test; data are mean \pm s.e.m. *P*-values are indicated.

To examine spontaneous motor activity, we scored limb-use bias. Uninjured mice used both limbs with relatively equal frequency, whereas unilaterally lesioned mice showed preferential ipsilateral touches, indicating disabled contralateral forelimb function. In lesioned mice transduced with AAV-shPTB, we observed a time-dependent improvement in contralateral forelimb use, whereas mice transduced with AAV-empty did not show any improvement (Fig. 6c). These results demonstrate essentially full correction of the motor phenotypes in this chemically induced model of Parkinson's disease. As Parkinson's disease and most other types of neurodegenerative diseases show age-dependent onset, we extended our approach from relatively young (two-month-old) mice to one-year-old mice, an age comparable to the age of onset of Parkinson's disease in humans. Of note, while the behavioural benefits of AAV-shPTB transduction following apomorphine-induced rotation did not reach statistical significance—perhaps owing to relatively unstable phenotype scored by this assay in aged animals (Fig. 6d)—a substantial improvement was recorded with the limb-use asymmetry test (Fig. 6e). These observations point to an age-related decrease in neuronal reprogramming, a critical challenge to be met in future studies.

Chemogenetic analysis of new DA neurons

We used the DREADD platform²⁷—a chemogenetic approach—to test whether new DA neurons are directly responsible for the restoration

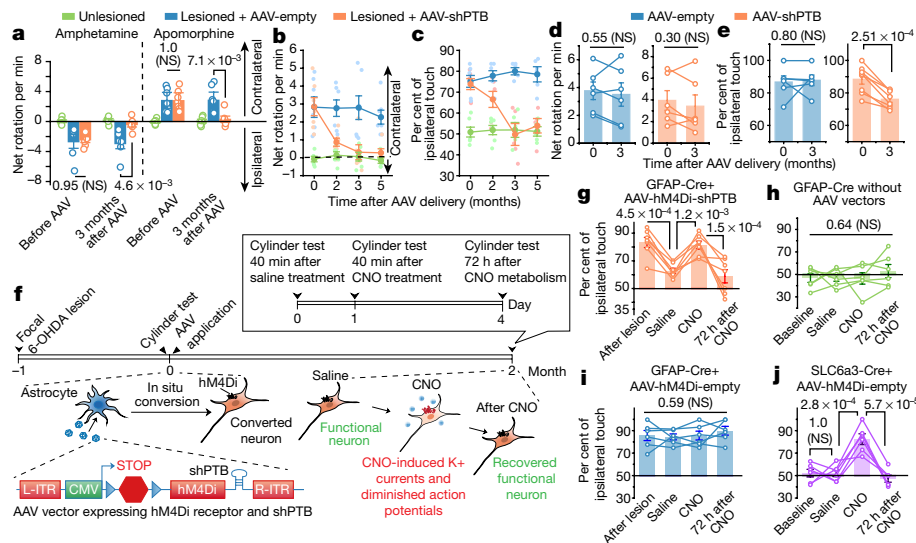


Fig. 6 | Behavioural benefits and chemical genetic evidence for induced neurons in brain repair. **a**, Behavioural study of mock-treated (green) or 6-OHDA-lesioned mice treated with AAV-empty (blue) or AAV-shPTB (orange). Rotation was induced by amphetamine (left) or apomorphine (right). $n = 7$ mice used for lesioned and treated conditions with AAV-empty or AAV-shPTB in apomorphine test; $n = 6$ mice for the other conditions. **b**, **c**, Time-course analysis of behavioural recovery. Rotation induced by apomorphine (**b**) and cylinder test for ipsilateral touches (**c**) in unilaterally lesioned mice ($n = 6$ or 7 mice analysed in each group, as in **a**). Data are mean \pm s.e.m. **d**, **e**, Apomorphine-induced rotation test (**d**) and cylinder test (**e**) on 1-year-old lesioned mice 3 months after treatment with AAV-empty or AAV-shPTB. $n = 8$ mice used for lesioned and treated conditions with AAV-shPTB in cylinder test; $n = 6$ mice for the other conditions. Circles represent individual mice; lines connect data from the same mouse before and after reprogramming. **f**, Schematic of the chemogenetic strategy to demonstrate that converted neurons are directly responsible for phenotypic recovery, emphasizing the rapid effect of injected CNO in inhibiting activities of reprogrammed neurons and reappearance of Parkinson's disease-like phenotype after CNO metabolism. **g**–**i**, Results of cylinder test before and after injecting AAV-hM4Di-shPTB and treatment with saline or CNO or 3 days after drug withdrawal (**g**) in unlesioned mice mock-treated or treated with CNO (**h**) or lesioned mice treated with AAV-hM4Di-empty vector (**i**). $n = 7$ *Gfap-cre* mice for **g**; $n = 6$ for **h**, **i**, **j**. The cylinder test results on unlesioned *Slc6a3* transgenic mice ($n = 6$) treated with AAV-hM4Di, which specifically targets endogenous DA neurons owing to DA neuron-restricted Cre expression via the *Slc6a3* promoter. Statistical significance was determined by ANOVA with post hoc Tukey test (**a**, **g**–**j**) or Student's *t*-test (**d**, **e**) and is presented as mean \pm s.e.m. *P*-values are indicated.

of motor function (Fig. 6f). We replaced RFP in our AAV-shPTB vector with a gene encoding an engineered inhibitory muscarinic receptor variant hM4Di, which responds to clozapine-*N*-oxide (CNO) instead of acetylcholine²⁸. As with the original AAV-shPTB, expression of both hM4Di and shPTB was activated in astrocytes in *Gfap-cre* mice. Neurons converted from astrocytes would be expected to incorporate this receptor into their plasma membrane and respond to CNO to activate G_i signalling, leading to hyperpolarization and suppression of electrical activity²⁹. CNO is metabolized 2 to 3 days after administration to allow functional restoration of hM4Di-expressing neurons²⁹.

As expected, the limb-use bias test indicated that motor performance of *Gfap-cre* mice with 6-OHDA lesions was restored two months after AAV-hM4Di-shPTB transduction. The lesion-induced phenotype reappeared within 40 min of intraperitoneal injection of CNO, but not with saline; moreover, the CNO-provoked motor phenotype disappeared within three days (Fig. 6g). CNO injection into uninjured mice had no effect, indicating that the drug did not affect endogenous DA neurons (Fig. 6h). AAV-hM4Di-empty showed no benefit to mice with lesions and had no effect on uninjured mice with or without CNO treatment (Fig. 6i, Extended Data Fig. 13d), demonstrating that the improvement in behaviour observed with AAV-hM4Di-shPTB was dependent on reprogramming.

Targeted expression of hM4Di in endogenous DA neurons (by injecting AAV-hM4Di-empty into the midbrain of mice expressing Cre from the DA neuron-specific *Slc6a3* gene promoter) was sufficient to induce the Parkinson's disease-like phenotype, but only in the presence of CNO (Fig. 6j), indicating that the introduction of the receptor into endogenous DA neurons had the intended CNO-mediated inactivating effect. Collectively, these data provide strong evidence that activity-induced

signalling by astrocyte-derived neurons is responsible for phenotypic recovery.

ASO-based neuronal conversion and rescue

The PTB-regulatory loop is self-reinforcing once it is triggered by initial PTB knockdown (Fig. 1a). In response to a reduction in PTB, miR-124 becomes more efficient at targeting *REST* (owing to the ability of PTB to directly compete with the miRNA-targeting site in the 3'-untranslated region of the mRNA encoded by *REST*), resulting in decreased levels of *REST*, which drives further de-repression of miR-124 and thus further suppression of PTB^{9,10}. This suggested that transient suppression of PTB might be sufficient to generate new neurons through ASO-mediated PTB mRNA degradation by intranuclear RNase H¹². We thus synthesized and screened PTB ASOs containing a phosphorothioate backbone¹² and a 3' fluorescein. An ASO targeting GFP served as control. Three PTB ASOs, but not GFP ASO, reduced PTB expression upon transfection into mouse astrocytes (Fig. 7a). The best targeting PTB ASO (no. 4), but not GFP ASO, induced expression of multiple neuronal markers, including TUJ1, MAP2, NSE and NeuN, after 5 weeks (Fig. 7b). A fraction of converted neurons were dopaminergic, as indicated by TH staining (Fig. 7b). Patch clamp recording showed that these in vitro-converted neurons were functional (Extended Data Fig. 14a–c).

We next injected PTB ASO or control GFP ASO into the midbrain of transgenic mice carrying a tamoxifen-inducible Cre that was selectively expressed in astrocytes and a tdTomato-encoding gene activated by Cre (Extended Data Fig. 14d, e). We induced Cre in these mice at P35 and stereotactically injected ASOs unilaterally into their substantia nigra 2 weeks later. PTB ASO converted a fraction of tdTomato-labelled cells to NeuN+ neurons after 8 weeks (Fig. 7c) and to TH+ neurons after

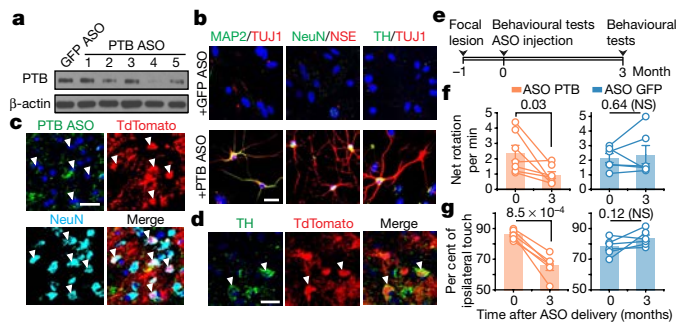


Fig. 7 | Proof-of-concept experiments with the ASO-based strategy. **a**, Screening for PTB ASOs by western blotting in mouse astrocytes. **b**, Neurons in isolated mouse cortical astrocytes induced with PTB ASO *in vitro* (**b**) stained for TUJ1 and MAP2 (left), NSE and NeuN (middle); a small fraction of converted neurons stained positively for TH (right). In **a**, **b**, $n = 3$ biological repeats. Scale bar, 20 μm . **c**, **d**, A proportion of tdTomato-labelled cells became NeuN+ by 8 weeks (**c**) and TH+ by 12 weeks (**d**) after injection of PTB ASO into the midbrain of *Gfap-creERTM; Rosa-tdTomato* transgenic mice. In **c**, **d**, $n = 4$ biological repeats. Scale bar, 20 μm . **e**–**g**, Schematic of 6-OHDA induced lesion, ASO treatment and behavioural tests (**e**) and results of apomorphine-induced rotation (**f**) and cylinder (**g**) tests. Circles represent individual mice; lines connect readings from the same mice before and after reprogramming ($n = 7$ used for lesioned and treatment with PTB ASO in apomorphine test; $n = 6$ for the other conditions; wild-type C57BL/6 mice). In **f**, **g**, two-sided Student's *t*-test. *P*-values are indicated.

12 weeks (Fig. 7d). Patch clamp recording demonstrated that these *in vivo*-converted neurons displayed functional neurophysiological properties (Extended Data Fig. 14f–i). Most notably, PTB ASO, but not control GFP ASO, rescued the 6-OHDA lesion-induced phenotype 3 months after injection, on the basis of both apomorphine-induced rotation and ipsilateral touch bias tests (Fig. 7e–g).

In summary, we report a one-step strategy to convert brain astrocytes to functional neurons. Our approach takes advantage of the genetic underpinnings of a neuronal differentiation program that is present, but latent in astrocytes. Taking advantage of the regional specificity of neuronal reprogramming, we efficiently converted midbrain astrocytes into functional DA neurons that integrate into the nigrostriatal dopamine pathway. Applying this approach to a chemically induced model of Parkinson's disease, we demonstrated partial replenishment of lost DA neurons and the restoration of striatal dopamine, leading to reversal of motor deficits. Notably, our ASO-based experiments illustrate a potentially clinically feasible approach for treatment of patients with Parkinson's disease. Eventual application of our approach to humans will need to overcome many obstacles, including age-related limits of reprogramming, understanding potential adverse effects caused by local astrocyte depletion (although we only converted only a small fraction of injury-induced astrocytes), specifically targeting regions that harbour vulnerable neurons, and detecting potential side effects due to mistargeted neurons. Each of these objectives can now be addressed experimentally to develop this promising therapeutic strategy—one that may be applicable to not only Parkinson's disease, but also other neurodegenerative disorders.

Note added in proof: While our work was under review, conceptually related results appeared elsewhere³⁰.

Online content

Any methods, additional references, Nature Research reporting summaries, source data, extended data, supplementary information,

acknowledgements, peer review information; details of author contributions and competing interests; and statements of data and code availability are available at <https://doi.org/10.1038/s41586-020-2388-4>.

- Poewe, W. et al. Parkinson disease. *Nat. Rev. Dis. Primers* **3**, 17013 (2017).
- Barker, R. A., Götz, M. & Parmar, M. New approaches for brain repair—from rescue to reprogramming. *Nature* **557**, 329–334 (2018).
- Sonntag, K. C. et al. Pluripotent stem cell-based therapy for Parkinson's disease: current status and future prospects. *Prog. Neurobiol.* **168**, 1–20 (2018).
- Cohen, D. E. & Melton, D. Turning straw into gold: directing cell fate for regenerative medicine. *Nat. Rev. Genet.* **12**, 243–252 (2011).
- Yu, X., Nagai, J. & Khakh, B. S. Improved tools to study astrocytes. *Nat. Rev. Neurosci.* **21**, 121–138 (2020).
- Rivetti di Val Cervo, P. et al. Induction of functional dopamine neurons from human astrocytes *in vitro* and mouse astrocytes in a Parkinson's disease model. *Nat. Biotechnol.* **35**, 444–452 (2017).
- Wu, Z. et al. Gene therapy conversion of striatal astrocytes into GABAergic neurons in mouse models of Huntington's disease. *Nat. Commun.* **11**, 1105 (2020).
- Gascón, S., Masserdotti, G., Russo, G. L. & Götz, M. Direct Neuronal Reprogramming: Achievements, Hurdles, and New Roads to Success. *Cell Stem Cell* **21**, 18–34 (2017).
- Xue, Y. et al. Direct conversion of fibroblasts to neurons by reprogramming PTB-regulated microRNA circuits. *Cell* **152**, 82–96 (2013).
- Xue, Y. et al. Sequential regulatory loops as key gatekeepers for neuronal reprogramming in human cells. *Nat. Neurosci.* **19**, 807–815 (2016).
- Hu, J., Qian, H., Xue, Y. & Fu, X. D. PTB/nPTB: master regulators of neuronal fate in mammals. *Biophys. Rep.* **4**, 204–214 (2018).
- Bennett, C. F., Krainer, A. R. & Cleveland, D. W. Antisense Diseases. *Annu. Rev. Neurosci.* **42**, 385–406 (2019).
- Guo, Z. et al. *In vivo* direct reprogramming of reactive glial cells into functional neurons after brain injury and in an Alzheimer's disease model. *Cell Stem Cell* **14**, 188–202 (2014).
- Lu, T. et al. REST and stress resistance in ageing and Alzheimer's disease. *Nature* **507**, 448–454 (2014).
- Li, Q. et al. The splicing regulator PTBP2 controls a program of embryonic splicing required for neuronal maturation. *eLife* **3**, e01201 (2014).
- Laywell, E. D., Rakic, P., Kukekov, V. G., Holland, E. C. & Steindler, D. A. Identification of a multipotent astrocytic stem cell in the immature and adult mouse brain. *Proc. Natl Acad. Sci. USA* **97**, 13883–13888 (2000).
- Sofroniew, M. V. Transgenic techniques for cell ablation or molecular deletion to investigate functions of astrocytes and other GFAP-expressing cell types. *Methods Mol. Biol.* **814**, 531–544 (2012).
- Tateno, T. & Robinson, H. P. The mechanism of ethanol action on midbrain dopaminergic neuron firing: a dynamic-clamp study of the role of I(h) and GABAergic synaptic integration. *J. Neurophysiol.* **106**, 1901–1922 (2011).
- Kimm, T., Khalil, Z. M. & Bean, B. P. Differential regulation of action potential shape and burst-frequency firing by BK and Kv2 Channels in substantia nigra dopaminergic neurons. *J. Neurosci.* **35**, 16404–16417 (2015).
- Boisvert, M. M., Erikson, G. A., Shokhirev, M. N. & Allen, N. J. The aging astrocyte transcriptome from multiple regions of the mouse brain. *Cell Rep.* **22**, 269–285 (2018).
- Nott, A. et al. Brain cell type-specific enhancer-promoter interactome maps and disease-risk association. *Science* **366**, 1134–1139 (2019).
- Grelish, S. et al. Human ESC-derived dopamine neurons show similar preclinical efficacy and potency to fetal neurons when grafted in a rat model of Parkinson's disease. *Cell Stem Cell* **15**, 653–665 (2014).
- Thiele, S. L., Warre, R. & Nash, J. E. Development of a unilaterally-lesioned 6-OHDA mouse model of Parkinson's disease. *J. Vis. Exp.* **60**, 3234 (2012).
- Beal, M. F. Parkinson's disease: a model dilemma. *Nature* **466**, S8–S10 (2010).
- Stott, S. R. & Barker, R. A. Time course of dopamine neuron loss and glial response in the 6-OHDA striatal mouse model of Parkinson's disease. *Eur. J. Neurosci.* **39**, 1042–1056 (2014).
- Boix, J., Padel, T. & Paul, G. A partial lesion model of Parkinson's disease in mice—characterization of a 6-OHDA-induced medial forebrain bundle lesion. *Behav. Brain Res.* **284**, 196–206 (2015).
- Zhu, H. & Roth, B. L. DREADD: a chemogenetic GPCR signaling platform. *Int. J. Neuropsychopharmacol.* **18**, pyu007 (2015).
- Armbruster, B. N., Li, X., Pausch, M. H., Herlitze, S. & Roth, B. L. Evolving the lock to fit the key to create a family of G protein-coupled receptors potentially activated by an inert ligand. *Proc. Natl Acad. Sci. USA* **104**, 5163–5168 (2007).
- Chen, Y. et al. Chemical control of grafted human PSC-derived neurons in a mouse model of Parkinson's disease. *Cell Stem Cell* **18**, 817–826 (2016).
- Zhou, H. et al. Glia-to-neuron conversion by CRISPR-CasRx alleviates symptoms of neurological disease in mice. *Cell* **181**, 590–603 (2020).

Publisher's note Springer Nature remains neutral with regard to jurisdictional claims in published maps and institutional affiliations.

© The Author(s), under exclusive licence to Springer Nature Limited 2020

Methods

Vectors and virus production

To build the lentiviral vector to express shPTB in mouse astrocytes, the target sequence 5'-GGGTGAAGATCCTGTCAATA-3' was shuttled into the pLKO.1-hygromycin vector (Addgene, #24150). To express shPTB in human astrocytes, the target sequence 5'-GCGTGAAGATCCTGTCAATA-3' was used. Viral particles were packaged in Lenti-X 293T cells (Takara bio) co-transfected with the two package plasmids: pCMV-VSV-G (Addgene, #8454) and pCMV-dR8.2 dvpr (Addgene, #8455). Viral particles were concentrated by ultracentrifugation in a Beckman XL-90 centrifuge with SW-28 rotor at 20,000 rpm for 120 min at 4 °C.

To construct AAV vectors, the same target sequence against mouse PTB was first inserted into the pTRIPZ-RFP vector (Dharmacon) between the EcoRI and Xho I sites. The segment containing RFP and shPTB was next subcloned to replace CaMP3.0 in the Asc I-digested AAV-CMV-LOX-STOP-LOX-mG-CaMP3.0 vector (Addgene, #50022). The empty vector contains only RFP subcloned into the same vector. To construct a control vector expressing non-target shRNA, the shPTB was replaced with 5'-CAACAAGATGAAGAGACCAA-3' to target GFP. The resulting vectors are referred to as AAV-shPTB, AAV-empty or AAV-shGFP. The AAV-hm4Di-shPTB vector was constructed by replacing RFP in AAV-shPTB with the cDNA of hm4Di, which was subcloned from pAAV-CBA-DIO-hm4Di-mCherry vector (Addgene, #81008). To express RFP and shPTB under the GFAP promoter, a segment containing floxed/off RFP and shPTB was used to replace eGFP in the AAV-GFAP-eGFP vector (Addgene, #50473) between the Sall and HindIII sites.

Viral particles of AAV2 were packaged in co-transfected HEK293T cells with the other two plasmids: pAAV-RC and pAAV-Helper (Agilent Genomics). After collection, viral particles were purified with a heparin column (GE Healthcare) and then concentrated with an Ultra-4 centrifugal filter unit (Amicon, 100,000 molecular weight cut-off). Titters of viral particles were determined by quantitative PCR to achieve $> 1 \times 10^{12}$ particles per ml.

Synthesis of antisense oligonucleotides

ASOs were synthesized by Integrated DNA Technologies. The sequence of the target region in mouse PTB for ASO synthesis is 5'-GGGTGAAGATCCTGTCAATA-3', and the target sequence in Turbo GFP is 5'-CAACAAGATGAAGAGACCAA-3'. The backbones of all ASOs contain phosphorothioate modifications. Fluorescein was attached to the 3' end of those ASOs for fluorescence detection.

Western blot and RT-qPCR

For western blotting, cells were lysed in 1× SDS loading buffer, and after quantification, bromophenol blue was added to a final concentration of 0.1%. Protein (25–30 µg) was resolved in 10% Nupage Bis-Tris gels and probed with the primary antibodies listed in the Supplementary Table 3.

For RT-qPCR, total RNA was extracted with Trizol (Life Technology) and 10 µg ml⁻¹ of glycogen was used to enhance precipitation of small RNAs. Total RNA was first treated with DNase I (Promega) followed by reverse transcription with the miScript II RT Kit (QIAGEN, 218160, for microRNA analysis) or the SuperScript III First-Strand Synthesis System (ThermoFisher, 18080051, for mRNA analysis). RT-qPCR was performed using the miScript SYBR Green PCR Kit (QIAGEN, 218073 for microRNA) or the Luna Universal qPCR Master Mix (NEB, M3003L, for mRNA) on a Step-One Plus PCR instrument (Applied Biosystems). The primers used are listed in Supplementary Table 4.

Cell culture and transdifferentiation in vitro

Mouse astrocytes were isolated from postnatal (P4–P5) pups. Cortical or midbrain tissue was dissected from whole brain and incubated with trypsin before plating onto dishes coated with poly-D-lysine (Sigma). Isolated astrocytes were cultured in DMEM (GIBCO) plus 10% fetal

bovine serum (FBS) and penicillin/streptomycin (GIBCO). Dishes were carefully shaken daily to eliminate non-astrocytic cells. After reaching ~90% confluency, astrocytes were disassociated with Accutase (Innovative Cell Technologies) followed by centrifugation for 3 min at 800 rpm, and then cultured in astrocyte growth medium containing DMEM/F12 (GIBCO), 10% FBS (GIBCO), penicillin/streptomycin (GIBCO), B27 (GIBCO), 10 ng ml⁻¹ epidermal growth factor (EGF, PeproTech), and 10 ng ml⁻¹ fibroblast growth factor 2 (FGF2, PeproTech).

To induce transdifferentiation in vitro, mouse astrocytes were resuspended with astrocyte culture medium containing the lentivirus that targets mouse PTB, and then plated on Matrigel Matrix (Corning)-coated coverslips (12 mm). After 24 h, cells were selected with hygromycin B (100 µg ml⁻¹, Invitrogen) in fresh astrocyte culture medium for 72 h. The medium was then switched to N3/basal medium (1:1 mix of DMEM/F12 and neurobasal medium, 25 µg ml⁻¹ insulin, 50 µg ml⁻¹ transferrin, 30 nM sodium selenite, 20 nM progesterone, 100 nM putrescine) supplemented with 0.4% B27, 2% FBS, a cocktail of 3 small molecules (1 µM ChIR99021, 10 µM SB431542 and 1 mM Db-cAMP), and neurotrophic factors (brain-derived neurotrophic factor, glial cell-derived neurotrophic factor, neurotrophin 3 and ciliary neurotrophic factor, all at 10 ng ml⁻¹). The medium was half-changed every the other day. To measure synaptic currents, converted cells after 5–6 weeks were added with fresh GFP-labelled rat astrocytes, and after a further 2–3 weeks of co-culture, patch clamp recordings were performed. To test the effect of PTB ASO in vitro, mouse astrocytes were cultured in six-well plates with astrocyte growth medium. When cells reached 70%–80% confluency, PTB ASO or GFP ASO (75 pmol per well) were transfected with Lipofectamine RNAimax (ThermoFisher Scientific). Forty-eight hours after ASO treatment, cells were either collected for immunoblotting or switched to N3/basal medium for further differentiation.

Human astrocytes were purchased from Cell Applications (taken from cerebral cortex at the gestational age of 19 weeks). Cells were grown in astrocyte medium (Cell Applications) and sub-cultured until they reached ~80% confluency. For transdifferentiation in vitro, cultured human astrocytes were first disassociated with trypsin, resuspended in astrocyte medium containing the lentivirus that targets human PTB, and plated on Matrigel Matrix-coated coverslips. After 24 h, cells were selected with hygromycin B (100 µg ml⁻¹, Invitrogen) for 72 h. The medium was switched to N3/basal medium supplemented with 0.4% B27, 2% FBS and neurotrophic factors (brain-derived neurotrophic factor, glial cell-derived neurotrophic factor, neurotrophin 3 and ciliary neurotrophic factor, all at 10 ng ml⁻¹). To measure synaptic currents, converted cells after three weeks were added with fresh GFP-labelled rat astrocytes, and after a further two to three weeks of co-culture, patch clamp recordings were performed.

Other cell lines used were checked for morphology using microscopy and immunostaining with specific markers. HEK293T cells were from a common laboratory stock. Lenti-X 293T cells were purchased from Takara Bio (#632180). MEFs were isolated from E14.5 C57BL/6 mouse embryos. Mouse neurons were isolated from E17–E18 C57BL/6 mouse embryos. Human dermal fibroblasts were purchased from ATCC (PCS-201-012). Human neurons were transdifferentiated from human neuronal progenitor cells, which were a gift A. Muotri (University of California, San Diego). All cell lines tested negative for mycoplasma contamination by Hoechst staining of the cells.

RNA-seq and data analysis

Total RNA was extracted from cultured cells with the Direct-zol RNA MiniPrep kit (Zymo Research). RNA-seq was performed as previously described³¹. In brief, 2 µg of total RNA was first converted to cDNA by the superscript III first-strand synthesis kit with primer Biotin-B-T. The cDNA was purified with a PCR Clean-Up Kit (Clontech) column to remove free primer and enzyme. Terminal transferase (NEB) was applied to block the 3' end of cDNA. Streptavidin-coated magnetic beads (Life Technologies) were used to isolate cDNAs. After RNA

Article

degradation by sodium hydroxide, the second-strand was synthesized by random priming and then eluted from beads by heat denaturing. The cDNA was then used as template to construct RNA-seq libraries. Sequencing was run on the HiSeq 4000 system. Low-quality reads were filtered and adaptors trimmed by using the software cutadapt with parameters “-a A{10} -m 22” (ref. ³²). Cleaned reads were mapped to the pre-indexed mm10 transcriptome using the software Salmon with parameters “quant -lA -validateMappings -seqBias” (ref. ³³). Raw counts of each library were applied to the R package DESeq2 for analysis of differentially expressed genes (DEGs) with false-discovery rate < 0.05, and hierarchical clustering was performed as described³⁴. The raw data from RNA-seq experiments have been deposited into NCBI under the accession number GSE142250.

Immunocytochemistry

Cultured cells grown on glass slides were fixed with 4% paraformaldehyde (PFA, Affymetrix) for 15 min at room temperature followed by permeabilization with 0.1% Triton X-100 in PBS for 15 min on ice. After washing twice with PBS, cells were blocked in PBS containing 3% BSA for 1 h at room temperature. Fixed cells were incubated with primary antibodies (listed in Supplementary Table 3) overnight at 4 °C in PBS containing 3% BSA. After washing twice with PBS, cells were incubated with secondary antibodies conjugated to Alexa Fluor 488, Alexa Fluor 546, Alexa Fluor 594 or Alexa Fluor 647 (1:500, Molecular Probes) for 1 h. DAPI (300 nM in PBS) was applied to cells for 20 min at room temperature to label nuclei. After washing three times with PBS, Fluoromount-G mounting medium was applied onto the glass slides, and images were examined and recorded under Olympus FluoView FV1000. Counting of cell numbers and percentages were all based on multiple biological replicates as detailed in specific figure legends.

For staining brain sections, mice were killed with CO₂ and immediately perfused, first with 15–20 ml saline (0.9% NaCl) and then with 15 ml 4% PFA in PBS to fix tissues. Whole brains were extracted and fixed in 4% PFA overnight at 4 °C, and then cut into 14–18 μm sections on a cryostat (Leica). Before staining, brain sections were incubated with sodium citrate buffer (10 mM sodium citrate, 0.05% Tween 20, pH 6.0) for 15 min at 95 °C for antigen retrieval. The slides were next treated with 5% normal donkey serum and 0.3% Triton X-100 in PBS for 1 h at room temperature. The remaining steps were performed as with cultured cells on coverslips.

Quantification of neuronal cell body and fibre density

Coronal sections across midbrain were sampled at intervals of 120–140 μm for immunostaining of TH and RFP. The total number (N_t) of cell types of interest was calculated by the stereological method, correcting with the Abercrombie formula³⁵. The formula used is $N_t = N_s \times (S_t/S_s) \times M/(M+D)$, where N_s is the number of neurons counted, S_t is the total number of sections in the brain region, S_s is the number of sections sampled, M is the thickness of section, and D is the average diameter of counted cells, as previously described^{36,37}.

RFP+ and RFP+TH+ fibres were quantified using a previously published sphere method²². For analysing striatal fibres, three coronal sections (A/P: +1.3, +1.0 and +0.70) were selected from each brain³⁶. For analysis of fibres in the nigrostriatal bundle, the coronal section closed to position Bregma –1.6 mm was selected. For each selected section, three randomly chosen areas were captured from one section of z-stack images at intervals of 2 μm using a 60× oil-immersion objective. A sphere (diameter: 14 μm) was then generated as a probe to measure fibre density within the whole z-stack. Each fibre crossing the surface of sphere was given a score. All images were analysed using Image-J 1.47v^{38,39}.

Electrophysiological recording

Patch clamp recordings were performed with Axopatch-1D amplifiers or Axopatch 200B amplifier (Axon Instruments) connecting to a Digidata1440A interface (Axon Instruments). Data were acquired with

pClamp 10.0 or Igor 4.04 software and analysed with MatLab v2009b. For neurons in vitro converted from mouse astrocytes, small molecules were removed from medium 1 week before patch clamp recording. Both cultured mouse and human cells were first incubated with oxygenated (95% O₂ and 5% CO₂) artificial cerebrospinal fluid (150 mM NaCl, 5 mM KCl, 1 mM CaCl₂, 2 mM MgCl₂, 10 mM glucose, 10 mM HEPES, pH 7.4) at 37 °C for 30 min and whole-cell patch clamp was performed on selected cells.

For recording activities of in vivo converted neurons, cortical slices (300 μm) were prepared 6 or 12 weeks after injection of AAV. Brain slices were prepared with a vibratome in oxygenated (95% O₂ and 5% CO₂) dissection buffer (110.0 mM choline chloride, 25.0 mM NaHCO₃, 1.25 mM NaH₂PO₄, 2.5 mM KCl, 0.5 mM CaCl₂, 7.0 mM MgCl₂, 25.0 mM glucose, 11.6 mM ascorbic acid, 3.1 mM pyruvic acid) at 4 °C followed by incubation in oxygenated artificial cerebrospinal fluid (aCSF) (124 mM NaCl, 3 mM KCl, 1.2 mM NaH₂PO₄, 26 mM NaHCO₃, 2.4 mM CaCl₂, 1.3 mM MgSO₄, 10 mM dextrose and 5 mM HEPES; pH 7.4) at room temperature for 1 h before experiments.

Patch pipettes (5–8 MΩ) solution contained 150 mM KCl, 5 mM NaCl, 1 mM MgCl₂, 2 mM EGTA–Na, and 10 mM Hepes pH 7.2. For voltage-clamp experiments, the membrane potential was typically held at –75 mV. The following concentrations of channel blockers were used: PiTX: 50 μM; NBQX: 20 μM; APV: 50 μM. All of these blockers were applied to the bath following dilution into the external solution from concentrated stock solutions. All experiments were performed at room temperature.

Transgenic mice

The *Gfap-cre* transgenic mouse (B6.Cg-Tg(*Gfap-cre*)77.6Mvs/2j) was used in AAV-shPTB induced in vivo reprogramming experiments. The Slc6a3-Cre transgenic mouse (B6.SJL-Slc6a3tm1.1(cre)Bkmm/J) was used for chemogenetic experiments. For testing the effect of ASOs in vivo, the *Gfap-creERTM* mouse (B6.Cg-Tg(*Gfap-cre/ERT2*)505Fmv/J) was crossed with the Rosa-tdTomato mouse (B6.Cg-Gt(ROSA)26Sortm14(CAG-tdTomato)Hze/J). Offspring of these double *Gfap-CreERTM; Rosa-tdTomato* transgenic mice at age P30–P40 days were injected with tamoxifen (dissolved in corn oil at a concentration of 20 mg ml⁻¹) via intraperitoneal injection once every 24 h for a total of 5 consecutive days. The dose of each injection was 75 mg kg⁻¹. Two weeks after tamoxifen administration, PTB ASO or control ASO was injected into substantia nigra of those mice to investigate ASO-induced in vivo reprogramming.

All transgenic mice were purchased from The Jackson Laboratory. All procedures were conducted in accordance with the guide of The University of California San Diego Institutional Animal Care and Use Committee (protocol no. S99116). Both male and female mice were used and randomly grouped in this study. No pre-tests were performed to determine sample sizes. Most studies used mice aged P30–P40. As indicated in Fig. 6d, e, mice at 1 year of age were also tested for AAV-shPTB-mediated reprogramming and behavioural tests.

Ipsilateral lesion with 6-OHDA and stereotaxic injections

Adult WT and *Gfap-cre* mice at P30–P40 were used to perform surgery to induce lesion. Animals were anaesthetized with a mix of ketamine (80–100 mg/kg) and xylazine (8–10 mg/kg) and then placed in a stereotaxic mouse frame. Before injecting 6-hydroxydopamine (6-OHDA, Sigma), mice were treated with a mix of desipramine (25 mg/kg) and pargyline (5 mg/kg). 6-OHDA (3.6 μg per mouse) was dissolved in 0.02% ice-cold ascorbate/saline solution at a concentration of 15 mg/ml and used within 3 h. The toxic solution was injected into the medial forebrain bundle at the following coordinates (relative to bregma): anterior–posterior (A/P) = –1.2mm; medio-lateral (M/L) = 1.3mm and dorso-ventral (D/V) = 4.75mm (from the dura). Injection was applied in a 5 μl Hamilton syringe with a 33G needle at the speed of 0.1 μl/min. The needle was slowly removed 3 min after injection. Cleaning and suturing of the wound were performed after lesion.

AAVs or ASOs were injected into substantia nigra -30 days after 6-OHDA induced lesion. Four microlitres of AAV or 2 μ l of ASO (1 μ g μ l⁻¹) was injected into lesioned substantia nigra at the following coordinates A/P: -3.0 mm; M/L: 1.2 mm and D/V: 4.5 mm. Injections were made using the same syringe and needle, at a rate of 0.5 μ l min⁻¹. The needle was slowly removed 3 min after injection. For injecting AAV in striatum and visual cortex, the following coordinates were employed: A/P: +1.2 mm; M/L: 2.0 mm; D/V 3.0 mm (for striatum), and A/P: -4.5 mm; M/L: 2.7 mm; D/V: 0.35 mm (visual cortex).

Retrograde tracing

For retrograde tracing of the nigrostriatal pathway, *Gfap-cre* mice with or without 6-OHDA induced lesion were first injected with AAV-shPTB. 1 or 3 months after AAV delivery, green Retrobeads IX (Lumafuor) were unilaterally injected at two sites into the striatum on the same side of AAV injection, using following two coordinates: A/P: +0.5 mm, M/L: 2.0 mm; D/V: 3.0 mm; and A/P: +1.2 mm; M/L: 2.0 mm; D/V: 3.0 mm. Approximately 2 μ l of beads was injected. After 24 h, animals were killed and immediately perfused. Their brains were fixed with 4% PFA for sectioning and immunostaining.

Measurement of striatal dopamine

Dopamine levels in mouse striatum were measured by reverse-phase HPLC. The HPLC analysis was performed on an Agilent 1260 Infinity HPLC system with an Agilent Zorbax SB-C18 semi-prep column (ID 9.4 \times 250 mm, 5 μ m, 80 \AA) using a water/methanol gradient containing 0.1% formic acid. Each substance was characterized by retention time and 260 nm absorbance under a variable wavelength detector as previously described^{40,41}. Striatal samples were directly prepared from brain tissue. In brief, striatal dissection was carried out immediately after euthanization. After homogenization in 200 μ l of 0.1 M hydrochloric acid with a Squisher homogenizer, the sample was centrifuged (12,000g, 10 min, 4 $^{\circ}$ C). The resulting supernatant was filtered by a 0.2 μ m Nanosep MF centrifugal device and then analysed by HPLC^{41,42}. Investigators were blinded to group identity for measurements of striatal dopamine.

Amperometric dopamine recording

The amperometric recording of dopamine release in vivo was conducted, as described previously^{43,44}. Anaesthetized mice were fixed on a stereotaxic instrument (Narishige). Body temperature was monitored and maintained at 37 $^{\circ}$ C using a heating pad (KEL-2000). A bipolar stimulating electrode was implanted in the medial forebrain bundle (MFB: 2.1 mm AP, 1.1 mm ML, 4.0–5.0 mm DV). The recording carbon fibre electrode (7 μ m diameter, 400 μ m long) was implanted in the caudate putamen of dorsal striatum (CPU: 1.1 mm AP, 1.7 mm ML, 3.4 mm DV). An Ag–AgCl reference electrode was placed in the contralateral cortex. Electric stimulation was generated using an isolator (A395, WPI) as a train of biphasic square-wave pulses (0.6 mA, 1 ms duration, 36 pulses, 80 Hz). The carbon fibre electrode was maintained at 780 mV to oxidize the substance. The amperometric signal was amplified by a patch-clamp amplifier (PC2C, INBIO), low pass-filtered at 50 Hz and recorded by MBA-1 DA/AD unit v4.07 (INBIO). Investigators were blinded to group identity for measurements of dopamine release.

Amperometric recordings of dopamine release on dorsal striatum slices were conducted, as described previously^{45,46}. Anaesthetized mice were transcardially perfused with -20 ml ice-cold recording aCSF containing 110 mM C₅H₁₄NClO, 2.5 mM KCl, 0.5 mM CaCl₂, 7 mM MgCl₂, 1.3 mM NaH₂PO₄, 25 mM NaCO₃, 25 glucose (saturated with 95% O₂ and 5% CO₂). The brain was rapidly removed and cut into 300- μ m horizontal slices on a vibratome (Leica VT 1000s) containing ice-cold sectioning solution. Slices containing striatum were allowed to recover for 30 min in recording aCSF: 125 mM NaCl, 2.5 mM KCl, 2 mM CaCl₂, 1.3 mM MgCl₂, 1.3 mM NaH₂PO₄, 25 mM NaCO₃, 10 mM glucose (saturated with 95% O₂ and 5% CO₂) at 37 $^{\circ}$ C, and then kept at room temperature for recording.

Carbon fibre electrodes (7 μ m diameter, 200 μ m long) holding at 780 mV were used to measure dopamine release in striatum. The exposed carbon fibre electrode tip was completely inserted into the subsurface of the striatal slice at an angle of -30 $^{\circ}$. Single electrical field stimulation pulses (0.2 ms, 0.6 mA) were delivered through a bipolar platinum electrode (150 μ m in diameter) and generated by a Grass S88K stimulator (Astro-Med). The amperometric current (I_{amp}) was low-pass filtered at 100 Hz and digitized at 3.13 kHz. Off-line analysis was performed using Igor software (WaveMetrix). Amperometric recording in cultured cells was conducted as previously described⁴⁷. Reprogrammed neurons were pre-treated with 100 μ M 3,4-dihydroxyphenylalanine (L-DOPA) for 30 min for signal enhancement. During recording, carbon fibre electrodes (WPI, CF30-50) were held at +750 mV to measure dopamine release. For baseline recording, cells were kept in normal aCSF (150 mM NaCl, 5 mM KCl, 1 mM CaCl₂, 2 mM MgCl₂, 10 mM glucose, 10 mM HEPES, pH 7.4). The solution was then switched to a high potassium aCSF (130 mM NaCl, 25 mM KCl, 1 mM CaCl₂, 2 mM MgCl₂, 10 mM glucose, 10 mM HEPES, pH 7.4) to induce the release of dopamine. No spike-like events were detected when the electrode was held at -750 mV under the same conditions⁴⁷.

Behavioural testing

All behavioural tests were carried out 21–28 days after 6-OHDA induced lesion or 2, 3 and 5 months after the delivery of AAVs or ASOs. The investigators were not blinded to allocation during experiments and outcome assessment. For the rotation test, apomorphine-induced rotations in mice were recorded after intraperitoneal injection of apomorphine (Sigma, 0.5 mg kg⁻¹) under a live video system. Mice were injected with apomorphine (0.5 mg kg⁻¹) on two separate days before performing the rotation test (for example, if the test was to be performed on Friday, the mouse would be first injected on Monday and Wednesday), which aimed to prevent a 'wind-up' effect that could obscure the final results. Rotation was measured 5 min following the injection for 10 min, as previously described^{48,49} and only full-body turns were counted. Rotations induced by D-amphetamine (Sigma, 5 mg kg⁻¹) were determined in the same system^{50,51}. Data were expressed as net contralateral or ipsilateral turns per min.

To perform the cylinder test, mice were individually placed into a glass cylinder (diameter 19 cm, height 25 cm), with mirrors placed behind for a full view of all touches, as described^{26,48}. Mice were recorded under a live video system and no habituation of the mice to the cylinder was performed before recording. A frame-by-frame video player (KMPlayer v.4.0.7.1) was used for scoring. Only wall touches independently with the ipsilateral or the contralateral forelimb were counted. Simultaneous wall touches (touched executed with both paws at the same time) were not included in the analysis. Data are expressed as a percentage of ipsilateral touches in total touches.

For chemogenetic experiment, cylinder tests were carried out 21–28 days after 6-OHDA induced lesion and 2 months after the delivery of AAV-hM4Di-shPTB. In the later test, each animal was first injected with saline to record the baseline of recovery. Subsequent recording was performed 40 min after intraperitoneal injection of CNO (Biomol International, 4 mg kg⁻¹) or 72 h after metabolism of the drug²⁹.

Data analysis and statistics

The numbers (n) of biological replicates or mice are indicated in individual figure legends. The experiments were not randomized and no statistical methods were used to predetermine sample size. Experimental variations in each graph were represented as mean \pm s.e.m. All measurements were performed on independent samples. Independent t -test, one-way ANOVA and repeat-measurement ANOVA were employed for statistical analysis, as indicated in individual figure legends. For multiple comparisons, combining ANOVA, post hoc Tukey test was applied. Assumptions of normal data distribution and homoscedasticity were adopted in t -test and one-way ANOVA. All statistical tests were

two-sided. For Fig. 1b and Extended Data Fig. 1b, the original data were transformed to logarithm with base 10 for one-way ANOVA to fulfill the requirement of homoscedasticity. To estimate the effect size, Cohen's *d* for *t*-test and eta-squared (η^2) for one-way ANOVA were calculated as previously described^{52,53}. Statistical report for all figure panels is summarized in Supplementary Table 5.

Reporting summary

Further information on research design is available in the Nature Research Reporting Summary linked to this paper.

Data availability

RNA-seq data have been deposited in the NCBI Gene Expression Omnibus under accession number GSE142250. Independently generated data are available upon request. Methods have been converted into stepwise protocols and deposited in Protocol Exchange (doi:10.21203/rs.3.pex-902/v1). Repeats of individual experiments are summarized in Supplementary Table 2, which has been independently verified. All data generated or analysed in this study are included in this published article (and its Supplementary Information files).

31. Ouyang, H. et al. WNT7A and PAX6 define corneal epithelium homeostasis and pathogenesis. *Nature* **511**, 358–361 (2014).
32. Martin, M. Cutadapt removes adapter sequences from high-throughput sequencing reads. *EMBnet journal* **17**, 10–12 (2011).
33. Srivastava, A., Malik, L., Smith, T., Sudbery, I. & Patro, R. Alevin efficiently estimates accurate gene abundances from dscRNA-seq data. *Genome Biol.* **20**, 65 (2019).
34. Love, M. I., Huber, W. & Anders, S. Moderated estimation of fold change and dispersion for RNA-seq data with DESeq2. *Genome Biol.* **15**, 550 (2014).
35. Abercrombie, M. Estimation of nuclear population from microtome sections. *Anat. Rec.* **94**, 239–247 (1946).
36. Falk, T. et al. Vascular endothelial growth factor-B is neuroprotective in an in vivo rat model of Parkinson's disease. *Neurosci. Lett.* **496**, 43–47 (2011).
37. Baker, H., Joh, T. H. & Reis, D. J. Genetic control of number of midbrain dopaminergic neurons in inbred strains of mice: relationship to size and neuronal density of the striatum. *Proc. Natl Acad. Sci. USA* **77**, 4369–4373 (1980).
38. Kordower, J. H. et al. Neurodegeneration prevented by lentiviral vector delivery of GDNF in primate models of Parkinson's disease. *Science* **290**, 767–773 (2000).
39. Bahat-Stroomza, M. et al. Induction of adult human bone marrow mesenchymal stromal cells into functional astrocyte-like cells: potential for restorative treatment in Parkinson's disease. *J. Mol. Neurosci.* **39**, 199–210 (2009).
40. Liu, G., Chen, J. & Ma, Y. Simultaneous determination of catecholamines and polyamines in PC-12 cell extracts by micellar electrokinetic capillary chromatography with ultraviolet absorbance detection. *J. Chromatogr. B* **805**, 281–288 (2004).
41. De Benedetto, G. E. et al. A rapid and simple method for the determination of 3,4-dihydroxyphenylacetic acid, norepinephrine, dopamine, and serotonin in mouse brain homogenate by HPLC with fluorimetric detection. *J. Pharm. Biomed. Anal.* **98**, 266–270 (2014).
42. Tareke, E., Bowyer, J. F. & Doerge, D. R. Quantification of rat brain neurotransmitters and metabolites using liquid chromatography/electrospray tandem mass spectrometry and comparison with liquid chromatography/electrochemical detection. *Rapid Commun. Mass Sp.* **21**, 3898–3904 (2007).
43. Wang, S. R. et al. Role of vesicle pools in action potential pattern-dependent dopamine overflow in rat striatum in vivo. *J. Neurochem.* **119**, 342–353 (2011).
44. Xu, H. et al. Striatal dopamine release in a schizophrenia mouse model measured by electrochemical amperometry in vivo. *Analyst* **140**, 3840–3845 (2015).
45. Wang, C. et al. Synaptotagmin-11 is a critical mediator of parkin-linked neurotoxicity and Parkinson's disease-like pathology. *Nat. Commun.* **9**, 81 (2018).
46. Wang, L. et al. Modulation of dopamine release in the striatum by physiologically relevant levels of nicotine. *Nat. Commun.* **5**, 3925 (2014).
47. Caiazzo, M. et al. Direct generation of functional dopaminergic neurons from mouse and human fibroblasts. *Nature* **476**, 224–227 (2011).
48. Grealish, S., Mattsson, B., Draxler, P. & Björklund, A. Characterisation of behavioural and neurodegenerative changes induced by intranigral 6-hydroxydopamine lesions in a mouse model of Parkinson's disease. *Eur. J. Neurosci.* **31**, 2266–2278 (2010).
49. Piallat, B., Benazzouz, A. & Benabid, A. L. Subthalamic nucleus lesion in rats prevents dopaminergic nigral neuron degeneration after striatal 6-OHDA injection: behavioural and immunohistochemical studies. *Eur. J. Neurosci.* **8**, 1408–1414 (1996).
50. Dunnett, S. B., Björklund, A., Stenevi, U. & Iversen, S. D. Behavioural recovery following transplantation of substantia nigra in rats subjected to 6-OHDA lesions of the nigrostriatal pathway. *I. Unilateral lesions. Brain Res.* **215**, 147–161 (1981).
51. Iancu, R., Mohapel, P., Brundin, P. & Paul, G. Behavioral characterization of a unilateral 6-OHDA-lesion model of Parkinson's disease in mice. *Behav. Brain Res.* **162**, 1–10 (2005).
52. Cohen, J. *Statistical Power Analysis for the Behavioral Sciences* (Academic Press, 1988).
53. Cohen, J. Eta-squared and partial eta-squared in fixed factor ANOVA designs. *Educ. Psychol. Meas.* **33**, 107–112 (1973).

Acknowledgements We thank members of the Fu laboratory for cooperation, reagent sharing and insightful discussion during the course of this investigation and A. Muotri for the gift of the human embryonic stem cell-derived neural progenitors. D.W.C. received a salary from the Ludwig Institute for Cancer Research and is a Nomis Foundation Distinguished Scientist. Z.Z. and X.K. were supported by NSFC grants (31930061, 31761133016, 21790394 and 81974203). W.C.M. and X.-D.F. were supported by a grant from the Larry Hillblom Foundation (2019-A-006-NET). This work was supported by NIH grants (GM049369 and GM052872) to X.-D.F.

Author contributions H.Q. and X.-D.F. designed the study. H.Q. performed astrocyte isolation, stereotaxic injection, immunocytochemistry, electrophysiological measurements and behaviour tests. J.H., Y.X. and F.M. contributed to AAV vector construction, immunoblotting and immunocytochemistry and independently characterized astrocyte conversion in vitro. F.M. also contributed to the performance of behaviour tests. Z.L. and F.M. performed RNA-seq and data analysis. H.Q., X.Z., D.Z. and N.K.D. measured striatal dopamine levels. X.K. and Z.Z. recorded activity-induced dopamine release in live animals and on brain slices. S.F.D. supervised ASO design and testing. W.C.M. contributed to analysis and interpretation of neurological data. D.W.C. oversaw biochemical and immunocytochemistry experiments. R.M. independently showed that ASO-mediated suppression of PTB generated new neurons in wild-type mice. R.M. also checked all raw data and verified biological repeats of individual experiments. H.Q., S.F.D., W.C.M., D.W.C. and X.-D.F. wrote the paper.

Competing interests X.-D.F. is a founder of CurePharma. The University of California, San Diego has filed a patent application on neuronal reprogramming induced by inactivating PTB by any means for treatment of neurological disorders.

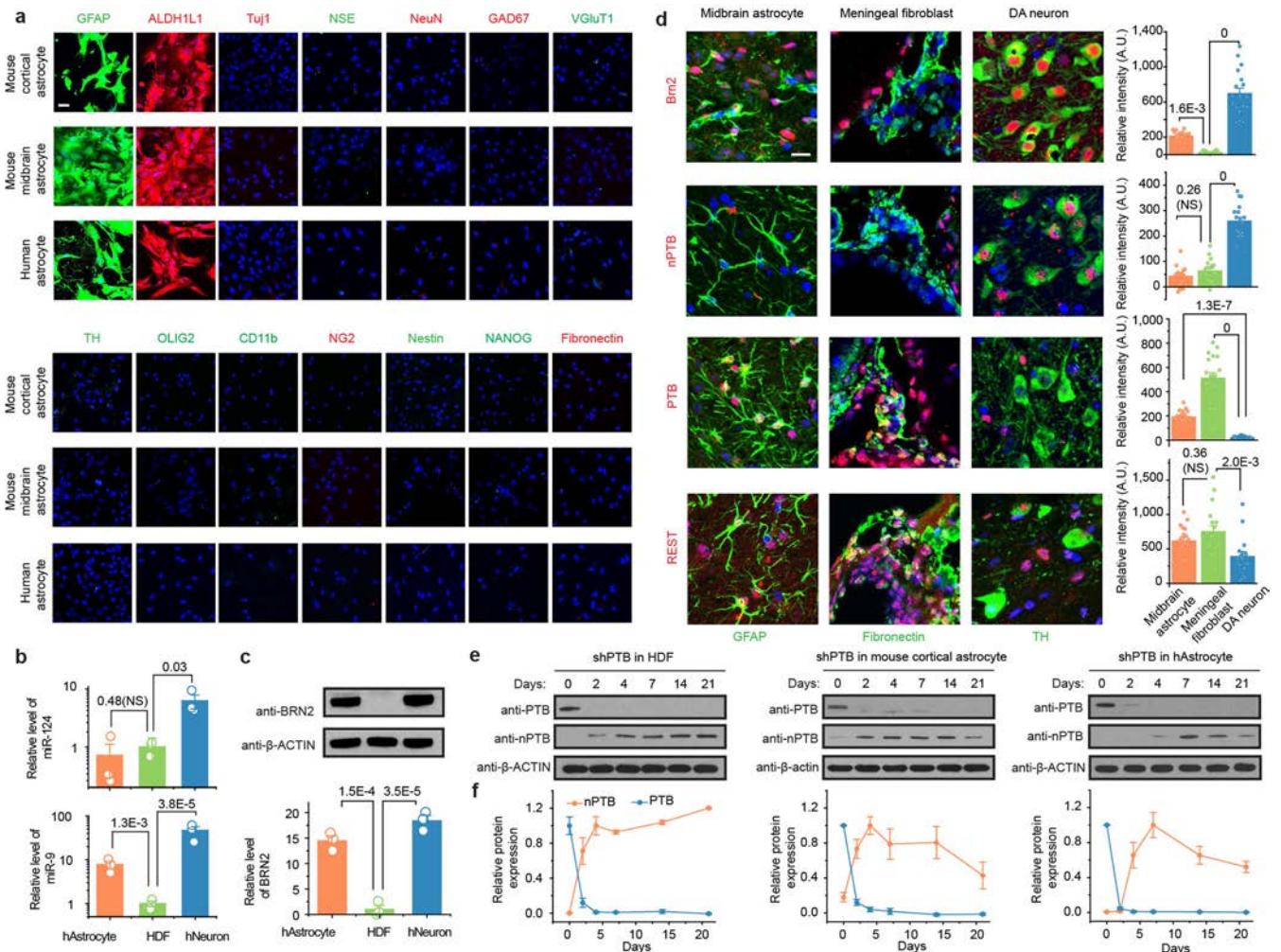
Additional information

Supplementary information is available for this paper at <https://doi.org/10.1038/s41586-020-2388-4>.

Correspondence and requests for materials should be addressed to X.-D.F.

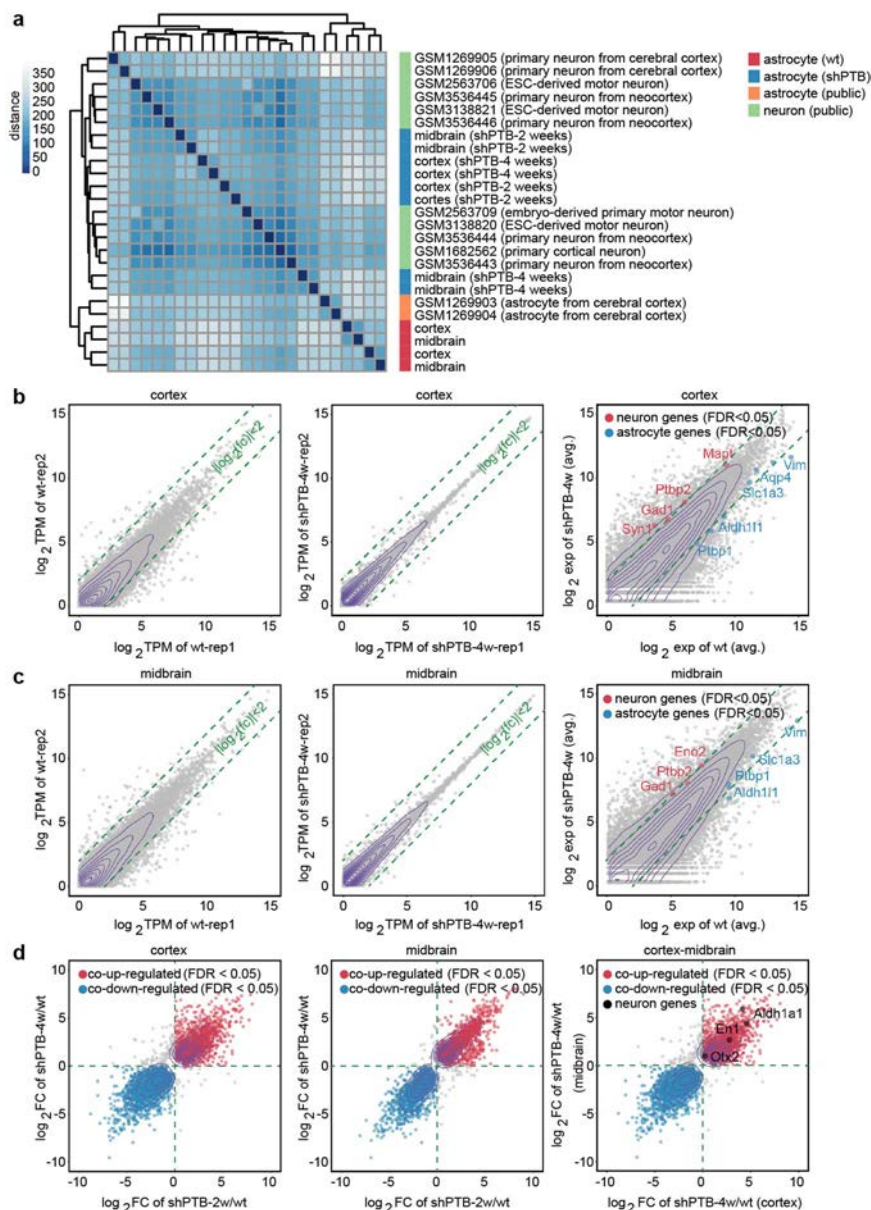
Peer review information Nature thanks Ernest Arenas, Anders Björklund, Aaron D. Gitler, Malin Parmar and the other, anonymous, reviewer(s) for their contribution to the peer review of this work.

Reprints and permissions information is available at <http://www.nature.com/reprints>.



Extended Data Fig. 1 | Characterization and functional analysis of astrocytes from mice and humans. **a**, Relative purity of mouse and human astrocytes. Astrocytes isolated from mouse cortex and midbrain or obtained from human embryonic brain (gestational age 19 weeks) were probed with a panel of markers for neurons and common non-neuronal cell types in the central nervous system, including those for astrocytes: GFAP (green) and ALDH1L1 (red); for neurons: *TUJ1*, NSE, NeuN, GAD67, VGluT1 and TH; for oligodendrocytes: OLIG2; for microglia: CD11b; for NG2 cells: NG2; for neural progenitors: nestin; for pluripotent stem cells: NANOG; and for fibroblasts: fibronectin. Scale bar, 30 μ m. These results demonstrated that isolated astrocytes are largely free of neurons and common non-neuronal cells. The experiment was independently repeated twice with similar results. **b**, **c**, Levels of key components in the regulatory loops controlled by PTB and nPTB in mouse midbrain. Levels of miR-124 (**b**, top) and miR-9 (**b**, bottom) were quantified by RT-qPCR in human astrocytes (hAstrocytes), human dermal fibroblasts (HDFs), and human neurons (hNeurons) differentiated from human neuronal progenitor cells. Data were normalized against U6 snRNA and the levels in human dermal fibroblasts were set to 1 for comparative analysis. Levels of BRN2 were determined by western blotting and normalized against β -actin (**c**). Results show low miR-124, but high miR-9 and BRN2 in human astrocytes,

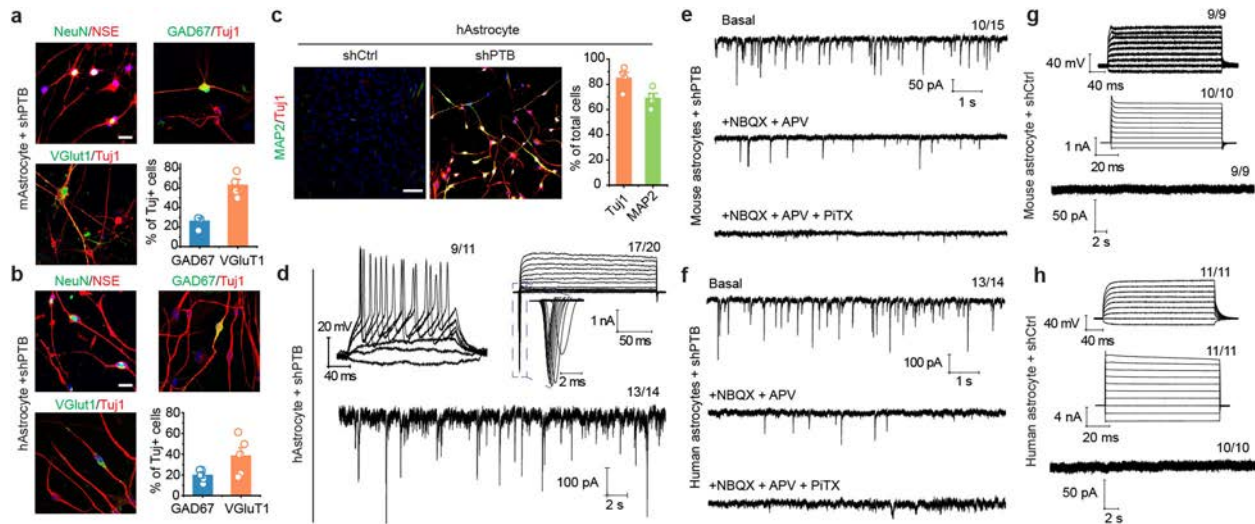
suggesting that the PTB-regulated loop is inactive and components of the nPTB-regulated loop are active in human astrocytes. **d**, Levels of PTB, nPTB, BRN2 and REST in mouse midbrain. Cell types in mouse midbrain were marked by GFAP for astrocytes, TH for DA neurons, and fibronectin for adjacent meningeal fibroblasts and double-stained for BRN2, PTB, nPTB and REST. Scale bar, 20 μ m. Relative immunofluorescence intensities in different cell types were quantified (right). $n = 3$ mice with a total of 54 cells counted in each. Note that REST is decreased, but not eliminated, in endogenous DA neurons, which is in agreement with the documented requirement for REST for viability of mature neurons. **e**, **f**, Dynamic nPTB expression in response to PTB knockdown. nPTB expression was monitored by western blotting after PTB knockdown in human dermal fibroblasts (**e**, left), mouse cortical astrocytes (**e**, middle) and human astrocytes (**e**, right). **f**, Data from 3 biological repeats were quantified. Results show that nPTB remains stably expressed in human dermal fibroblasts, but undergoes transient expression in astrocytes from both mice and humans. In **b–d**, ANOVA with post hoc Tukey test; mean \pm s.e.m. ($n = 3$ biological repeats). *P*-values are indicated. All except those pairwise comparisons indicated as NS (not significant) in panels **b** and **d** are considered statistically significant.



Extended Data Fig. 2 | Global evidence for programmed switch of gene expression from astrocytes to neurons in response to PTB depletion.

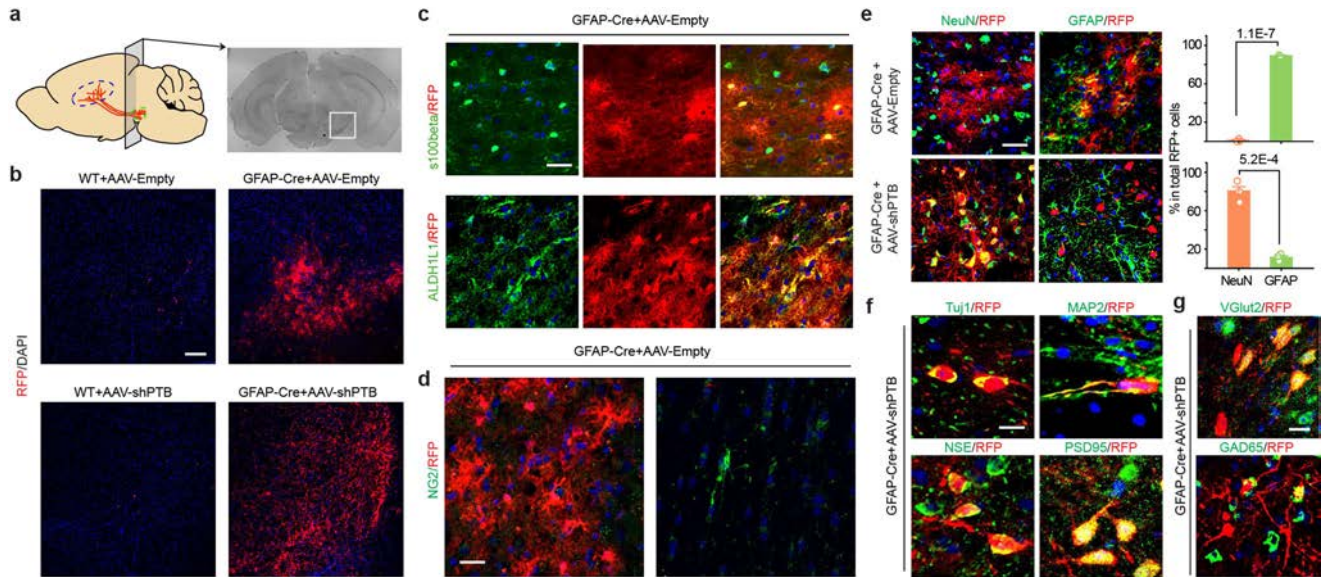
a, Clustering analysis. RNA-seq data (available under GSE142250) were generated on independent isolates of astrocytes from mouse cortex or midbrain before and after conversion to neurons by depleting PTB for 2 or 4 weeks. By clustering analysis, the global gene expression profiles were compared with the public datasets for astrocytes or neurons as indicated by the colour key and the data sources on the right. The selection of these public data for comparison was based on astrocytes without further culture and on neurons directly isolated from mouse brain or differentiated from embryonic stem cells (ESCs). **b, c**, Comparison of gene expression profiles between independent libraries prepared from mouse cortical (**b**) or midbrain (**c**) astrocytes before and after PTB depletion for 2 or 4 weeks. Selective

astrocyte-specific (blue) and neuron-specific (red) genes are highlighted. Results show a degree of heterogeneity between independent isolates of astrocytes, but notably, their converted neurons became more homogeneous. **d**, Comparison between induced gene expression upon PTB depletion in cortical versus midbrain astrocytes. Several commonly induced DA neuron-specific genes (that is, *Otx2*, *En1* and *Aldh1a1*) are highlighted when comparing between neurons derived from cortical versus midbrain astrocytes (right). Significantly induced DA neuron-associated genes are listed in Supplementary Table 1. Note that most genes are enriched, but not uniquely expressed, in DA neurons (thus, they are not specific markers for DA neurons), as evidenced by their induction to different degrees in shPTB-treated cortical astrocytes.



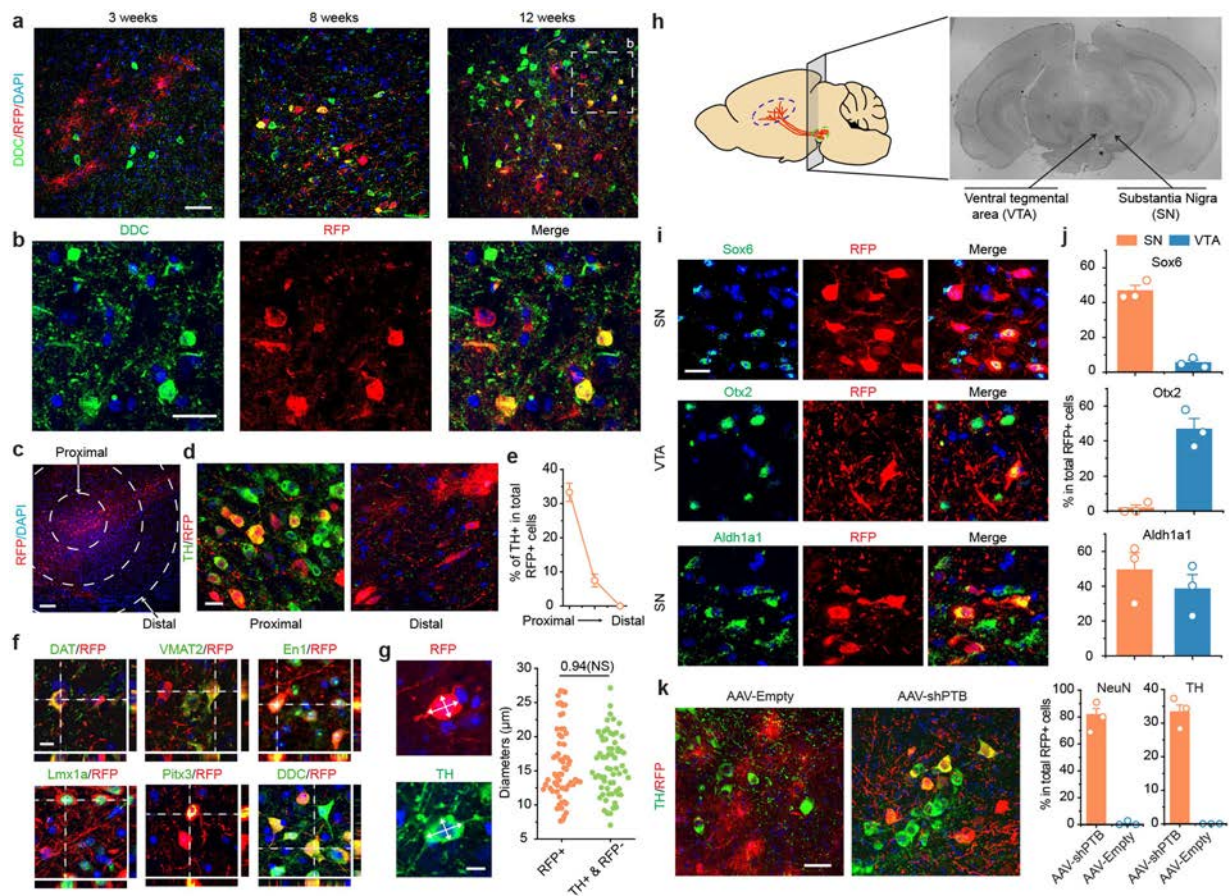
Extended Data Fig. 3 | Characterization of converted neurons from mouse and human astrocytes. **a, b**, Conversion of mouse and human astrocytes to neurons. Cells were immunostained with the indicated markers after conversion from mouse cortical astrocytes (**a**) or human astrocytes (**b**). Converted glutamatergic (marked by VGlut1) and GABAergic (marked by GAD67) neurons constituted approximately 90% and 80% of total TUJ1-marked neurons from mouse and human astrocytes, respectively. Data were based on 4 (**a**) or 5 (**b**) biological repeats and represented as mean \pm s.e.m. Scale bars, 30 μ m (**a**); 40 μ m (**b**). **c, d**, Efficient conversion from human astrocytes to neurons. Converted neurons were characterized by immunostaining with TUJ1 and MAP2 (**c**). Scale bar, 80 μ m. $n = 4$ biological repeats. **d**, These neurons are functional as indicated by repetitive action potentials (top left), large currents of voltage-dependent sodium and potassium channels (top right) and

spontaneous postsynaptic currents after co-culture with rat astrocytes (bottom). Indicated in each panel is the number of cells that showed the recorded activity versus the number of cells examined. **e–h**, Electrophysiological characterization of neurons converted from mouse (**e**) and human (**f**) astrocytes, showing spontaneous excitatory and inhibitory postsynaptic currents that could be sequentially blocked with the inhibitors against the excitatory (NBQX and APV) and inhibitory (PiTX) receptors, indicative of their secretion of glutamine and GABA neurotransmitters. **g, h**, Control shRNA (shCtrl)-treated mouse (**g**) and human (**h**) astrocytes failed to show action potentials (top), currents of voltage-dependent channels (middle) or postsynaptic events (bottom). The number of cells that showed the recorded activity versus the total number of cells examined is indicated on the top right of each panel.



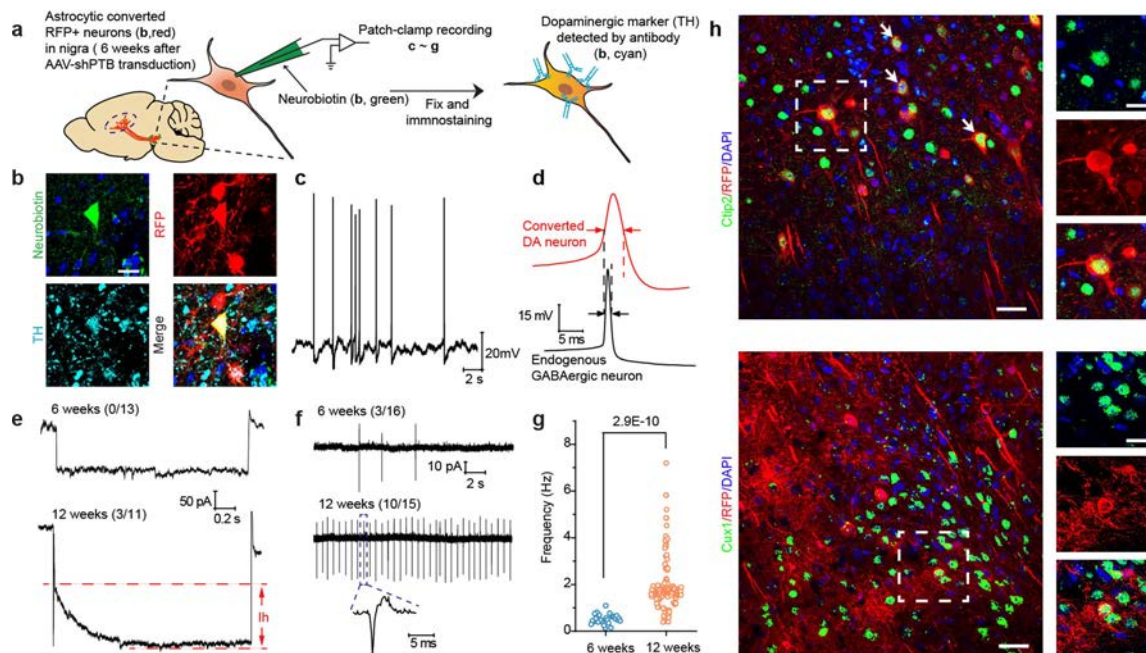
Extended Data Fig. 4 | Cre-dependent expression of RFP in injected mouse midbrain. **a**, Schematic of the substantia nigral region (white box) for AAV injection and immunochemical analysis. **b**, Cre-dependent RFP expression. RFP+ cells were not detected in midbrain of wild-type mice injected with either AAV-empty or AAV-shPTB (left). In comparison, both viruses generated abundant RFP signals in *Gfap-cre* transgenic mice. Scale bar, 150 μ m. **c**, **d**, Co-staining of RFP+ cells with the astrocyte markers S100b and ALDH1L1 10 weeks after injecting AAV-empty (c), indicating that most RFP+ cells in AAV-empty-transduced midbrain were astrocytes. Scale bar, 25 μ m. **d**, No RFP expression was detectable in NG2-labelled cells. Scale bar, 15 μ m. Experiments in **b-d** were independently repeated three times with similar results.

e, Reprogramming-dependent conversion from astrocytes to neurons. Immunostaining with the astrocyte marker GFAP and the pan-neuronal marker NeuN was performed 10 weeks after injection of AAV-empty or AAV-shPTB in the midbrain. Scale bar, 30 μ m. Quantified results show that cells transduced with AAV-empty were all GFAP+ astrocytes, whereas cells transduced with AAV-shPTB were mostly NeuN+ neurons. Quantified data were based on three mice as shown on the right. Two-sided Student's *t*-test. Data are mean \pm s.e.m. **f**, **g**, Further characterization of AAV-shPTB-induced neurons in midbrain with additional neuronal markers, including pan-neuronal specific markers TUJ1, MAP2, NSE and PSD95 (**f**; scale bar, 10 μ m) and specific markers for glutamatergic (VGlut2) and GABAergic (GAD65) neurons (**g**; scale bar, 20 μ m).



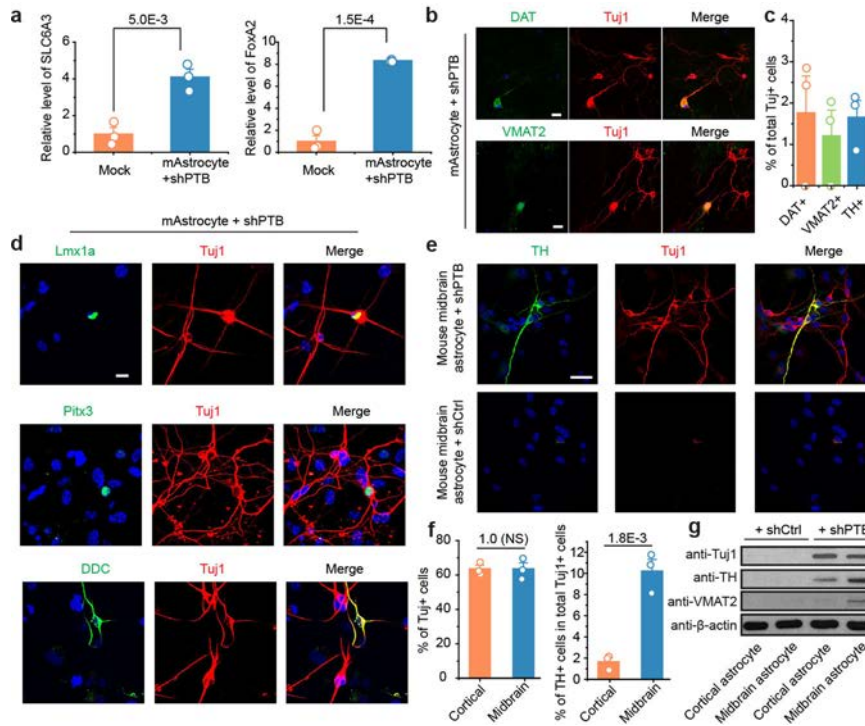
Extended Data Fig. 5 | Progressive conversion of AAV-shPTB treated astrocytes to DA neurons within the dopamine domain. **a, b**, Time-dependent appearance of RFP+DDC+ DA neurons. AAV-shPTB-transduced midbrain was characterized for time-dependent appearance of DA neurons with the DA neuron marker DDC (**a**; scale bar, 50 μm). Few initial RFP+ cells were co-stained with DDC 3 weeks after AAV-shPTB transduction, and the fraction of RFP+DDC+ cells progressively increased 8 and 12 weeks after AAV-shPTB injection. Images from substantia nigra 12 weeks after AAV-shPTB transduction are enlarged to highlight RFP+DDC+ neurons (**b**; scale bar, 25 μm). **c–e**, Conversion of midbrain astrocytes to DA neurons within the dopamine domain. AAV-shPTB-induced neuronal reprogramming was determined relative to the site of injection. **c**, A low-magnification view of a substantia nigra section. Circles mark brain areas with progressively larger diameters from the centre of the injection site. Scale bar, 100 μm . **d**, Enlarged views show the representative proximal and distal sites from the injection site 12 weeks after AAV-shPTB transduction, positively stained for TH (green) over RFP-labelled cells. Scale bar, 10 μm . Note the presence of RFP+TH+ cells in the proximal site, but only RFP+TH– cells in the distal site. **e**, The percentages of TH+ cells among total RFP+ cells in the three different areas defined in (**c**) were quantified based on 3 mice with at least 100 cells counted in each. Data are mean \pm s.e.m. These data show the generation of TH+ neurons within the dopamine domain of midbrain. **f, g**, Further characterization of converted DA neurons with additional DA neuron-specific markers DAT, VMAT2, EN1, LMX1A, PITX3 and DDC, all showing positive signals (**f**). RFP+TH+ cell bodies are highlighted by orthogonal views of z-stacked images, attached on right and

bottom of the main image (**f**; scale bar, 10 μm). Cell body diameters were compared between newly converted RFP+TH+ neurons and endogenous RFP–TH+ DA neurons (**g**, left; scale bar, 5 μm). The size distribution of both populations of neurons shown on the right suggests that converted TH+ cells have a similar cell size to endogenous TH+RFP– DA neurons (**g**, right). Quantification based on 62 RFP+ cells and 64 RFP–TH+ cells from 3 mice. Two-sided Student's *t*-test. **h**, Schematic depiction for further analysis of converted neurons in substantia nigra and ventral tegmental area. **i, j**, Representative immunostaining of SOX6, OTX2 and ALDH1A1, showing that SOX6-marked RFP+ cells were confined to the substantia nigra, whereas OTX2-marked RFP+ cells were in the ventral tegmental area; the DA neuron marker ALDH1A1 was detected in both substantia nigra and ventral tegmental area (**i**; scale bar, 25 μm). **j**, Quantification based on 3 mice with at least 100 cells counted. Data are mean \pm s.e.m. Results further support the generation of different subtypes of DA neurons. **k**, Minimal leaky Cre expression in endogenous DA neurons in midbrain. As *Gfap-cre* is known to show a degree of leaky expression in neurons, raising a concern that AAV-shPTB might infect some endogenous DA neurons, mice treated with AAV-empty (which expresses RFP but not shPTB) were examined carefully. Scale bar, 30 μm . Compared with AAV-shPTB treated mice, few RFP+ cells stained positively for either NeuN or TH in the midbrain of mice transduced with AAV-empty, as quantified on the right, based on 3 mice with at least 100 cells counted in each. Data are mean \pm s.e.m. Results show little, if any, leaky Cre expression in endogenous DA neurons and in midbrain regions of mice at the age (two months old) used in our studies.



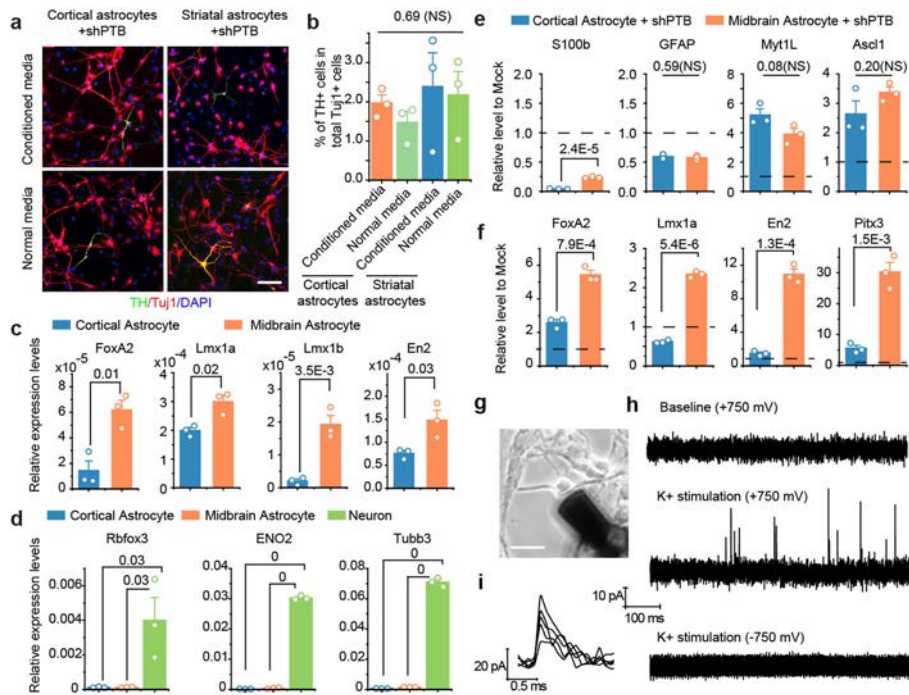
Extended Data Fig. 6 | Electrophysiological properties of gradually matured DA neurons. **a, b**, Schematic depiction of patch recording of converted neurons in midbrain (**a**). According to this scheme, the fluorescent dye Neurobiotin 488 (green) loaded in the electrode was used to mark cell bodies in substantia nigra for patch clamp recording on brain slices. **b**, After recording, the patched cells were confirmed to be RFP+TH+ to demonstrate the recording being performed on newly converted neurons (scale bar, 20 μ m). Experiments were independently repeated 4 times with similar results. **c–e**, Detection of spontaneous action potential (**c**) and relatively wider action potential generated by newly converted neurons in comparison with endogenous GABAergic neurons (**d**). **e**, Notably, hyperpolarization-activated currents of HCN channels (I_h currents) were recorded at 12 weeks after, but not 6 weeks after, AAV-shPTB-induced neuronal conversion; these currents could be specifically blocked with CsCl. The numbers of cells that showed the recorded activity versus the total number of cells examined are indicated. Note that the bottom trace is also shown in Fig. 2h. **f, g**, Extracellular recording

showing more converted neurons firing spontaneous action potentials at 12 weeks after transduction with AAV-shPTB than at 6 weeks after transduction. The numbers of cells that showed the recorded activity versus the total number of cells examined are indicated. **g**, The frequency of spontaneous spikes that increased upon further maturation was further quantified. Data were based on a total of 31 cells from 4 mice. Results show progressive maturation of newly converted DA neurons in the brain. Statistical significance was determined by two-sided Student's *t*-test. **h**, Cortical neurons generated in AAV-shPTB-transduced cortex, in contrast to a large population of RFP+TH+ cells in midbrain. As a control, AAV-shPTB was injected in cortex. After 12 weeks, RFP+ cells were co-stained with the cortical neuron marker CTIP2 (top) and CUX1 (bottom). Scale bars, 40 μ m (main); 15 μ m (magnified inset). Note that RFP+ CUX1+ cells are rare in comparison to RFP+CTIP2+ cells, indicative of different conversion efficiency in different layers of cortex. Experiments were independently repeated twice with similar results.



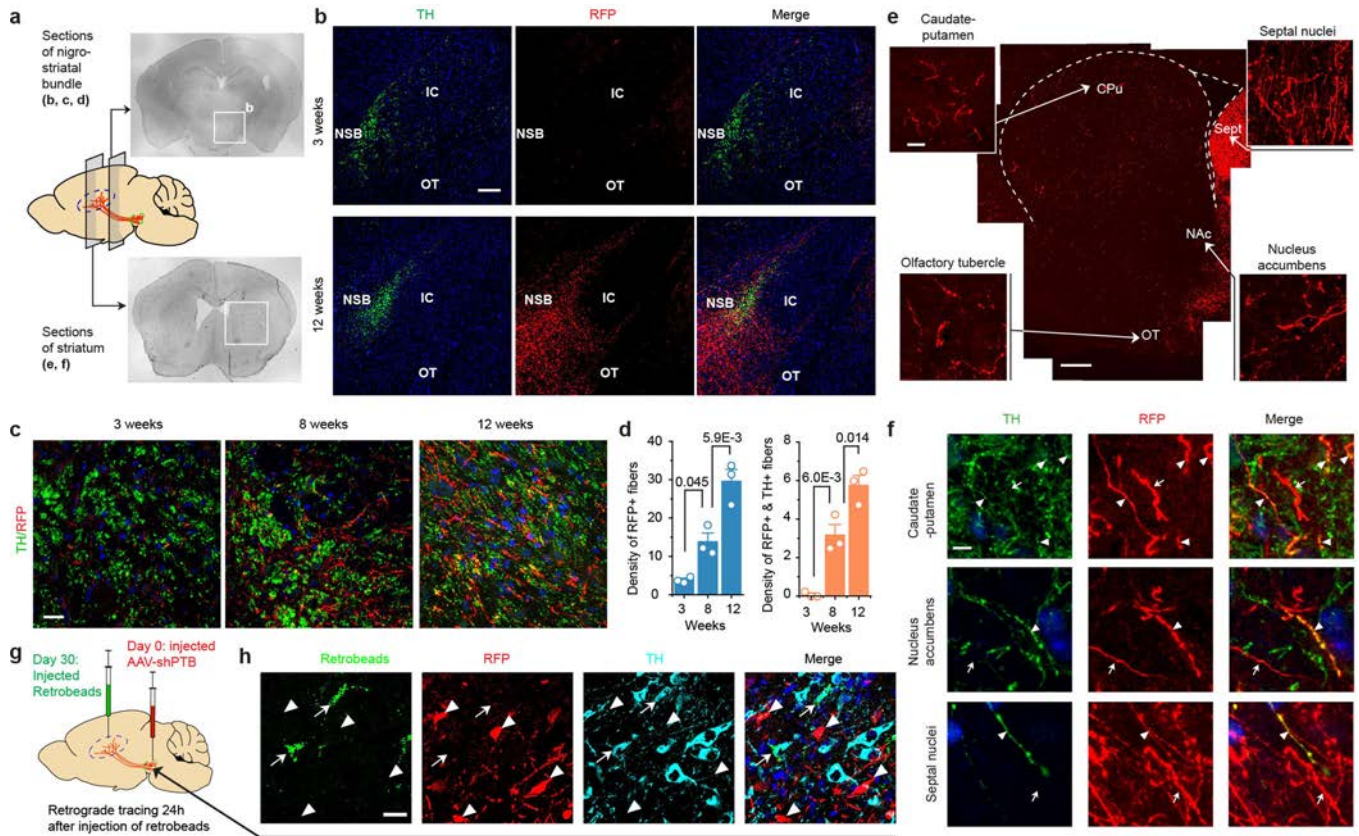
Extended Data Fig. 7 | Characterization of cortical astrocyte-derived neurons compared with midbrain astrocyte-derived neurons. **a–c**, A small fraction of cortical astrocyte-derived neurons express DA neuron markers. **a**, RT-qPCR showed the induction of DA neuron-specific genes *Slc6a3* and *Foxa2* in isolated cortical astrocytes treated with lentiviral shPTB. These DA-like neurons were further characterized by immunostaining for additional DA neuron markers DAT and VMAT2 (**b**; scale bar, 20 μ m) and quantified among TUJ1+ cells based on 3 biological repeats with at least 100 cells counted in each (**c**). Two-sided Student's *t*-test; mean \pm s.e.m. *P*-values are indicated. Results indicate that although cortex does not contain DA neurons and RFP+TH+ DA-like neurons were never detected in AAV-shPTB-transduced cortex in the brain, isolated cortical astrocytes were able to give rise to a fraction of DA-like neurons in vitro. This implies that astrocytes may become more plastic in culture than within specific brain environments. **d**, Additional immunochemical evidence for the expression of DA neuron-specific markers (LMX1A, PITX3 and DDC) in a subpopulation of TUJ1+ cells derived from cortical astrocytes. Scale bar, 20 μ m. Experiments were independently repeated 3 times with similar results. **e–g**, TH staining of TUJ1+ neurons derived

from midbrain astrocytes and comparison with neurons derived from cortical astrocytes. **e**, Lentiviral shPTB, but not control shRNA, converted midbrain astrocytes into TH+ DA neurons in culture. Scale bar, 25 μ m. **f**, Conversion efficiencies of cortical and midbrain astrocytes, showing similar high percentage of TUJ1+ neurons (left), but a significantly higher percentage of DA neurons converted from midbrain astrocytes compared with cortical astrocytes (right). Data are based on 3 biological repeats with at least 200 cells counted in each. Statistical significance was determined by two-sided Student's *t*-test; mean \pm s.e.m. *P*-values are indicated. **g**, Western blotting analysis of a pan-neuronal marker (TUJ1) and two specific markers for DA neurons (TH and VMAT2) in shPTB-reprogrammed astrocytes from cortex and midbrain, showing much higher levels of the DA neuron markers in neurons generated from midbrain astrocytes compared to cortical astrocytes. Experiments were independently repeated twice with similar results. Together, these data strongly suggest intrinsic cellular differences that are responsible for the generation of different neuron subtypes from astrocytes in different brain regions.



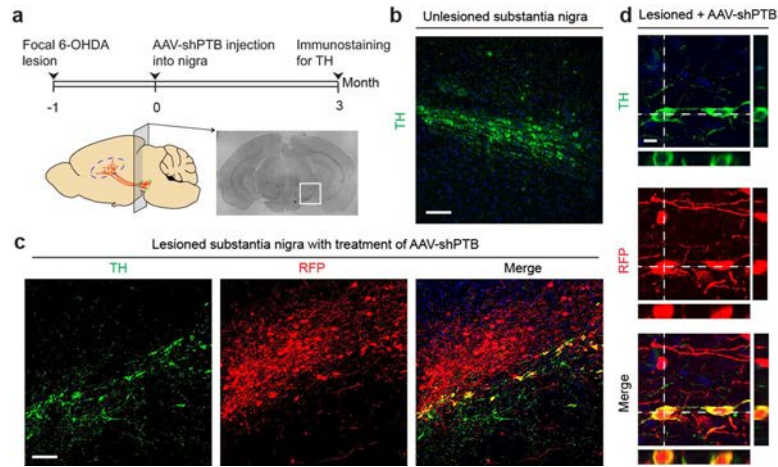
Extended Data Fig. 8 | Cell-autonomous mechanisms for the regional specificity in neuronal conversion. **a**, TH⁺ neurons generated from cortical astrocytes with normal and conditioned media from cultured midbrain astrocytes. Scale bar, 100 μ m. **b**, Quantification of cells in **a**. Three biological repeats with at least 100 cells counted in each. Statistical significance was determined by ANOVA; mean \pm s.e.m. **c-f**, RT-qPCR analysis of DA neuron-specific transcription factors in cortical and midbrain astrocytes before and after lentiviral shPTB-induced neuronal conversion. **c**, The indicated transcription factors were quantified by real-time PCR and normalized against β -actin mRNA. **d**, To ensure that the isolated astrocytes were free of contaminated neurons, RT-qPCR was also performed with the 3 indicated pan-neuron markers with isolated neurons as control. **e**, In response to PTB knockdown, astrocyte-specific genes *S100b* and *Gfap* were repressed, whereas pan-neuronal transcription factors *Myt1l* and *Ascl1* were activated in astrocytes derived from both cortex and midbrain. Dashed lines indicate levels before shPTB treatment, which was set to 1 for comparison with levels after

shPTB treatment. **f**, Under the same conditions, the 4 DA-neuron-specific transcription factors were more robustly induced in response to PTB depletion in midbrain astrocytes compared to cortical astrocytes. Statistical significance was determined by ANOVA with post hoc Tukey test (**d**) or two-sided Student's *t*-test (**c**, **e**, **f**), based on 3 biological repeats; mean \pm s.e.m. *P*-values are indicated. Results suggest higher basal levels and more robust induction of DA neuron-specific transcription factors in midbrain astrocytes compared to cortical astrocytes, providing evidence for the differences in cell-intrinsic gene expression programs in giving rise to distinct subtypes of neurons. **g-i**, Schematic of amperometric recording of monoamine release, showing the placement of a carbon fibre electrode on a midbrain astrocyte-derived neuron (**g**). Scale bar, 30 μ m. **h**, Spike-like events were captured by holding the electrode at +750 mV after K⁺ (25 mM) stimulation. **i**, A high-resolution view of dopamine release events in **h**. Results demonstrate a key functional property of midbrain astrocyte-derived DA neurons. Experiments were independently repeated twice with similar results.



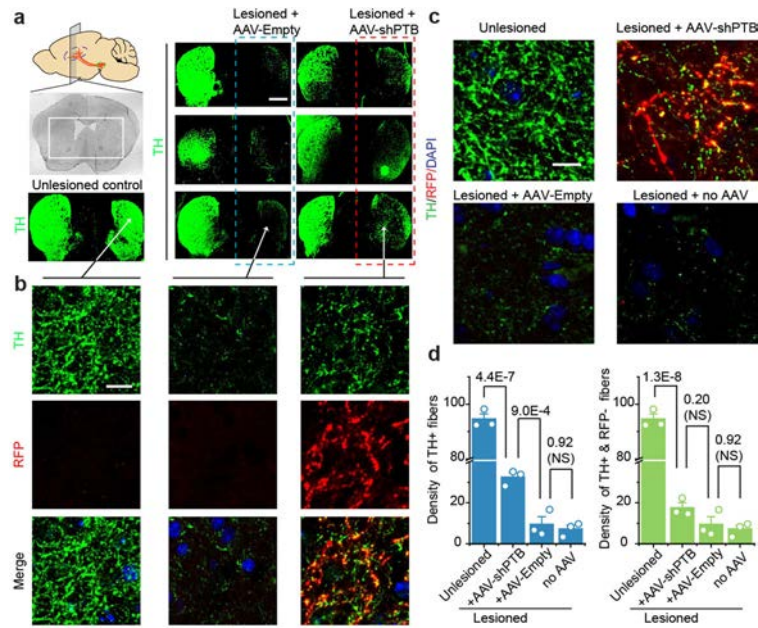
Extended Data Fig. 9 | Time-course analysis of fibre outgrowth from converted neurons. **a**, Schematic of coronal sections for analysing fibre density in the nigrostriatal pathway. **b-d**, Sphere-determined density of RFP+ fibres that were progressively increased along the nigrostriatal bundle (NSB). Shown are low-magnification views (**b**; scale bar, 150 μ m) and enlarged views (**c**; scale bar, 35 μ m). IC, internal capsule. **d**, Quantification of RFP+ (left) or RFP+TH+ fibres (right), based on 3 independent biological sections. Statistical significance was determined by ANOVA with post hoc Tukey test; mean \pm s.e.m. *P*-values are indicated. Results show time-dependent increase in fibre density, a portion of which also exhibits colocalization of the DA neuron marker TH. **e**, Low-magnification view of striatum innervated by RFP+ projections. Scale bar, 300 μ m. Smaller panels show magnified views of RFP+ projections in different regions. Scale bar, 15 μ m. Note the bright RFP signals in septal nuclei. **f**, Three selected regions were further amplified to highlight a fraction of RFP+ fibres with (arrowheads) or without (arrows) co-staining with the DA neuron

marker TH. Scale bar, 5 μ m. Results emphasize that converted DA neurons targeted broader regions in striatum than endogenous DA neurons, which might cause side effects—a potential caveat of neuronal reprogramming experiments that requires investigation in future studies. **g, h**, Retrograde tracing of TH+ neurons from striatum to substantia nigra. Depicted is the AAV-shPTB injection site at day 0 and the retrobead injection site at day 30 (**g**). Retrograde tracing was monitored 24 h after injection of retrobeads. After treatment with AAV-shPTB for 30 days, TH+ cells, but not TH+RFP+ cells, in substantia nigra were labelled with retrograde beads (**h**). Arrowheads, RFP+ cells; arrows, cell bodies of endogenous TH+ DA neurons labelled with retrograde beads. Scale bar, 20 μ m. These data provide a critical control for AAV-shPTB-converted DA neurons that could be traced from striatum to substantia nigra, as described in the main text. All experiments shown in this figure were independently repeated 3 times with similar results.



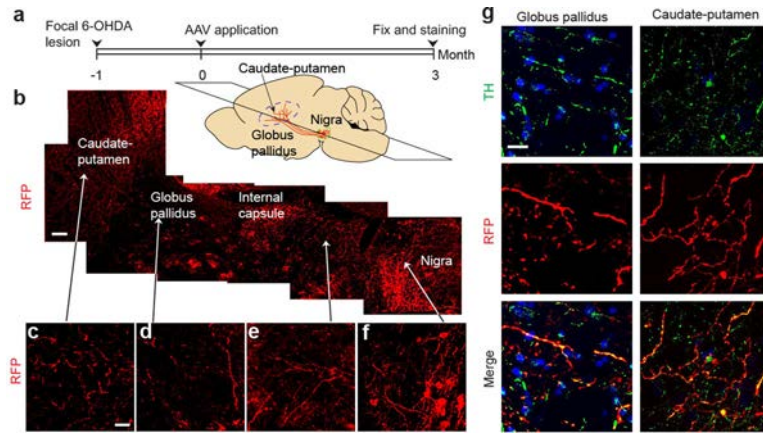
Extended Data Fig. 10 | shPTB-converted neurons replenish lost dopaminergic neurons in substantia nigra. **a**, Schematic of the experimental schedule for 6-OHDA-induced lesion followed by reprogramming with AAV-PTB and then TH staining. **b, c**, Low-magnification views of unlesioned substantia nigra stained for TH (**b**) and substantia nigra lesioned with 6-OHDA and transduced with AAV-shPTB (**c**). Scale bars, 80 μm . These data were used to provide the quantitative information shown in Fig. 4f, g. **d**, Enlarged view of

RFP+ cells that co-expressed TH in substantia nigra. Two RFP+TH+ cell bodies are highlighted by orthogonal views of z-stacked images, attached on the right and bottom of the main image in each panel. Scale bar, 10 μm . Results show the generation of TH+ DA neurons in a highly region-specific manner in substantia nigra, as a large population of RFP+ cells were not labelled by TH staining in the same image. All experiments shown in this figure were independently repeated 3 times with similar results.



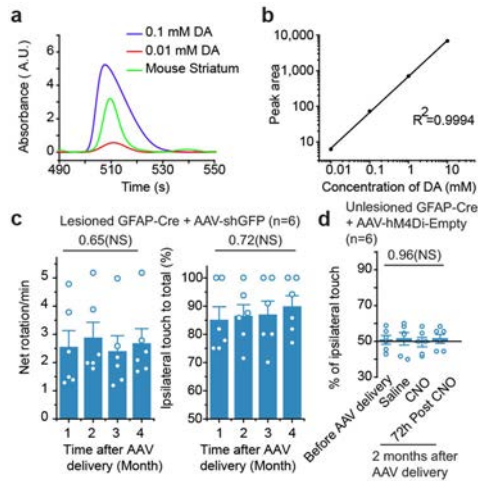
Extended Data Fig. 11 | Restoration of TH+ neurons in striatum of 6-OHDA-lesioned mice. a, b, Schematic of the coronal section of striatum and images of uninjured control and lesioned striatum treated on the right side of the brain with either AAV-empty or AAV-shPTB (a). Scale bar, 500 μm . **b,** Magnified images showed extensive colocalization of TH with RFP-labelled fibres. Scale bar, 10 μm . Results show a significant degree of restoration of TH+ fibres in striatum. Experiments were independently repeated 3 times with similar results. **c, d,** Quantitative analysis of TH+ fibres in striatum under different treatment conditions. TH staining of striatum under different

treatment conditions, as indicated (c). Scale bar, 10 μm . **d,** Quantification of total TH+ or TH+RFP- fibre density in striatum under different treatment conditions based on 3 biological repeats. Statistical significance was determined by ANOVA with post hoc Tukey test; mean \pm s.e.m. *P*-values are indicated. Results show that most TH+ fibres seem to derive from AAV-shPTB-converted dopaminergic neurons; however, the data do not rule out the possibility that the axons of some endogenous neurons also responded to the environment created by newly converted neurons.

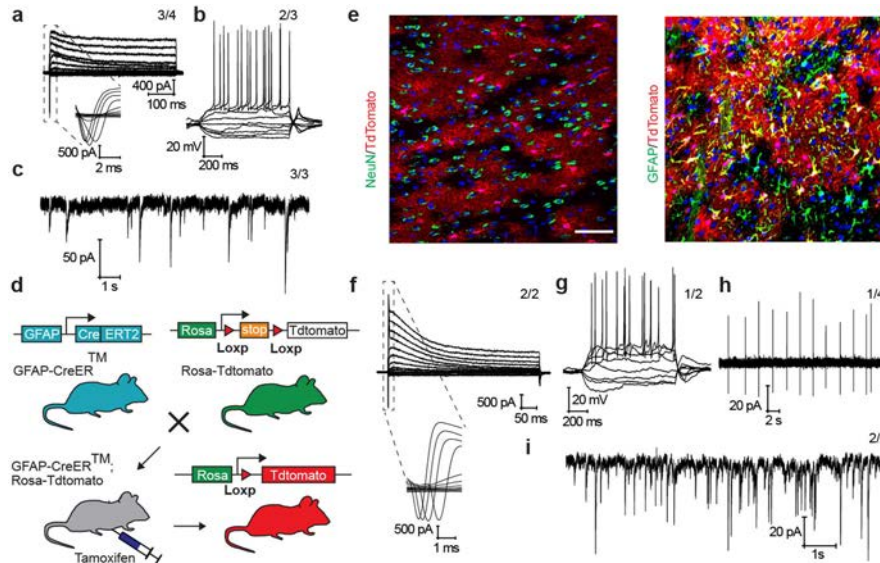


Extended Data Fig. 12 | Reconstruction of the nigrostriatal pathway by converted dopaminergic neurons. **a**, Schematic of the experimental schedule for 6-OHDA-induced lesion and reconstruction of the nigrostriatal pathway. **b–f**, Images of RFP+ projections extending from substantia nigra to striatum. The schematic diagram shows the dorso-ventral level of the

horizontal section. Scale bar, 100 μm . Magnified views show indicated brain regions (**c–f**). Scale bar, 25 μm . **g**, Amplified views of RFP-positive fibres that co-stained with TH in CPu and globus pallidus. Scale bar, 20 μm . These data were used to provide the quantitative information shown in Fig. 4h, i. Experiments were independently repeated twice with similar results.



Extended Data Fig. 13 | Measurement of striatal dopamine by HPLC and controls with AAV-shGFP and AAV-hM4Di. a, b, Dopamine levels in brain detected by HPLC with two different doses of spiked dopamine (**a**). **b**, Standard curve generated from the spiked dopamine. This set of experiments was performed only once. **c**, Controls for behavioural tests, showing that expressing an anti-GFP control shRNA alone did not rescue chemical-induced behavioural deficits based on apomorphine-induced rotation (left) and cylinder test (right). **d**, Controls for behavioural tests, showing that the expression of hM4Di in non-reprogrammed astrocytes did not trigger detectable behaviour change in non-lesioned mice in the presence of CNO. Statistical significance was determined by ANOVA (**c, d**); mean \pm s.e.m. Six mice were analysed in each group. *P*-values are indicated.



Extended Data Fig. 14 | Electrophysiological analysis of PTBASO-induced neurons in vitro and in brain. **a–c**, Converted neurons showed large currents from voltage-dependent sodium and potassium channels (**a**), repetitive action potentials (**b**) and spontaneous postsynaptic currents (**c**). The numbers of cells that showed the recorded activity versus the total number of cells examined are indicated on the top right in each panel. **d**, Schematic of transgenic mice used to trace astrocytes in vivo. **e**, Three weeks after tamoxifen treatment, none of the tdTomato-labelled cells in the midbrain of *Gfap-cre ER:Rosa-tdTomato* mice stained positive for NeuN (left), and all were GFAP+

(right). Scale bar, 50 μm . **f–i**, Converted neurons in brain slices showed large currents from voltage-dependent sodium and potassium channels (**f**), repetitive action potentials (**g**), spontaneous action potentials (**h**) and spontaneous postsynaptic currents (**i**). The numbers of cells that showed the recorded activity versus the total number of cells examined are indicated. The results show that functional neurons are induced by PTBASO both in culture and in mouse brain. All experiments shown in this figure were independently repeated twice with similar results.

Reporting Summary

Nature Research wishes to improve the reproducibility of the work that we publish. This form provides structure for consistency and transparency in reporting. For further information on Nature Research policies, see [Authors & Referees](#) and the [Editorial Policy Checklist](#).

Statistics

For all statistical analyses, confirm that the following items are present in the figure legend, table legend, main text, or Methods section.

n/a Confirmed

- The exact sample size (n) for each experimental group/condition, given as a discrete number and unit of measurement
- A statement on whether measurements were taken from distinct samples or whether the same sample was measured repeatedly
- The statistical test(s) used AND whether they are one- or two-sided
Only common tests should be described solely by name; describe more complex techniques in the Methods section.
- A description of all covariates tested
- A description of any assumptions or corrections, such as tests of normality and adjustment for multiple comparisons
- A full description of the statistical parameters including central tendency (e.g. means) or other basic estimates (e.g. regression coefficient) AND variation (e.g. standard deviation) or associated estimates of uncertainty (e.g. confidence intervals)
- For null hypothesis testing, the test statistic (e.g. F , t , r) with confidence intervals, effect sizes, degrees of freedom and P value noted
Give P values as exact values whenever suitable.
- For Bayesian analysis, information on the choice of priors and Markov chain Monte Carlo settings
- For hierarchical and complex designs, identification of the appropriate level for tests and full reporting of outcomes
- Estimates of effect sizes (e.g. Cohen's d , Pearson's r), indicating how they were calculated

Our web collection on [statistics for biologists](#) contains articles on many of the points above.

Software and code

Policy information about [availability of computer code](#)

Data collection Olympus FluoView Ver.4.2a, pClamp 10.0, Igor 4.04, MBA-1 DA/AD unit v4.07

Data analysis Image-J 1.47v, Clampfit 10.4, OriginPro 2016, KMPlayer v4.0.7.1, MatLab v2009b, R v3.5.1, cutadapt v2.8, salmon v0.14.1, DEseq2 v1.22.2

For manuscripts utilizing custom algorithms or software that are central to the research but not yet described in published literature, software must be made available to editors/reviewers. We strongly encourage code deposition in a community repository (e.g. GitHub). See the Nature Research [guidelines for submitting code & software](#) for further information.

Data

Policy information about [availability of data](#)

All manuscripts must include a [data availability statement](#). This statement should provide the following information, where applicable:

- Accession codes, unique identifiers, or web links for publicly available datasets
- A list of figures that have associated raw data
- A description of any restrictions on data availability

All data generated or analyzed during this study are included in this published article (and its supplementary information files). The raw data from RNA-seq experiments have been deposited into NCBI GEO under the accession number GEO: GSE142250.

Field-specific reporting

Please select the one below that is the best fit for your research. If you are not sure, read the appropriate sections before making your selection.

- Life sciences Behavioural & social sciences Ecological, evolutionary & environmental sciences

Life sciences study design

All studies must disclose on these points even when the disclosure is negative.

Sample size	No statistical analysis was employed to determine the sample size. The sample size was chosen base on previous publications using the same techniques.
Data exclusions	No data were excluded.
Replication	All key experiments in our manuscript have been repeated via intra- and inter-term collaboration and in different biological contexts. All statistical analysis were based on at least three replicates. More details of biological repeats are described in Supplementary Table 2.
Randomization	The mice used in all experiments were chosen randomly according to their unique identification numbers.
Blinding	Investigators were masked to group identity for measurements of striatal dopamine and dopamine release.

Reporting for specific materials, systems and methods

We require information from authors about some types of materials, experimental systems and methods used in many studies. Here, indicate whether each material, system or method listed is relevant to your study. If you are not sure if a list item applies to your research, read the appropriate section before selecting a response.

Materials & experimental systems

n/a	Involved in the study
<input type="checkbox"/>	<input checked="" type="checkbox"/> Antibodies
<input type="checkbox"/>	<input checked="" type="checkbox"/> Eukaryotic cell lines
<input checked="" type="checkbox"/>	<input type="checkbox"/> Palaeontology
<input type="checkbox"/>	<input checked="" type="checkbox"/> Animals and other organisms
<input checked="" type="checkbox"/>	<input type="checkbox"/> Human research participants
<input checked="" type="checkbox"/>	<input type="checkbox"/> Clinical data

Methods

n/a	Involved in the study
<input checked="" type="checkbox"/>	<input type="checkbox"/> ChIP-seq
<input checked="" type="checkbox"/>	<input type="checkbox"/> Flow cytometry
<input checked="" type="checkbox"/>	<input type="checkbox"/> MRI-based neuroimaging

Antibodies

Antibodies used	We provide the all the essential information for antibodies in Supplementary Table 3.
Validation	The antibodies used were validated by the previous publications or routine experimental protocols, listed in Supplementary Table 3.

Eukaryotic cell lines

Policy information about [cell lines](#)

Cell line source(s)	HEK293T cells were from a common laboratory stock. Lenti-X 293T cells were purchased from Takara Bio (#632180). Mouse Embryonic Fibroblasts (MEF) were isolated from E14.5 C57BL/6 mouse embryos. Mouse neurons were isolated from E17~18 C57BL/6 mouse embryos. Mouse astrocytes were isolated from P4~P5 C57BL/6 mouse brain (see METHODS). Human dermal fibroblasts (HDF) were purchased from ATCC (PCS-201-012). Human neurons were trans-differentiated from human neuronal progenitor cells, which is a gift from Dr.Alysson Muotri's lab. Human astrocytes were purchased from Cell Applications (882AK-05f).
Authentication	The cell lines used were checked for morphology by microscopy and immunostaining with specific markers.
Mycoplasma contamination	We periodically checked potential contamination with mycoplasma, which causes retarded cell growth and low pH in the media. All cell lines tested negative for mycoplasma contamination by Hoechst staining of the cells according to Young L.et al., Nature Protocols,2010.
Commonly misidentified lines (See ICLAC register)	No. The cell lines used are not listed in the database.

Animals and other organisms

Policy information about [studies involving animals](#); [ARRIVE guidelines](#) recommended for reporting animal research

Laboratory animals	All animal experiments were conducted in accordance with the guide of The University of California San Diego Institutional~40
--------------------	---

Laboratory animals

Animal Care and Use Committee (Protocol# S99116). Transgenic mice including B6.Cg-Tg(Gfap-cre)77.6Mvs/2J, B6.SJLSc6a3tm1.1(cre)Bkmn/J, B6.Cg-Tg(GFAP-cre/ERT2)505Fmv/J, and B6.Cg-Gt(ROSA)26Sortm14(CAG-tdTomato)Hze/J were purchased from The Jackson Laboratory. Both male and female mice were used in this study. All mice at age of postnatal day 30~40 were used. 1year old B6.Cg-Tg(Gfap-cre)77.6Mvs/2J mice were also used to perform surgery to induce lesion.

Wild animals

This study did not involve wild animals.

Field-collected samples

This study did not involve samples collected from the field.

Ethics oversight

All procedures were conducted in accordance with the guide of The University of California San Diego Institutional Animal Care and Use Committee.

Note that full information on the approval of the study protocol must also be provided in the manuscript.